An Application of Geosynthetic Cementitious Composite Mat for Slope Stabilization

Mr. Phong Tan Ngo

A Dissertation Submitted in Partial Fulfillment of the Requirements

for the Degree of Doctor of Philosophy Program in Civil Engineering

Department of Civil Engineering

Faculty of Engineering

Chulalongkorn University

Academic Year 2017

การประยุกต์ใช้แผ่นซีเมนต์ใยสังเคราะห์คอมโพสิตสำหรับเสถียรภาพของลาดดิน

นายฟง ทาน โง

วิทยานิพนธ์นี้เป็นส่วนหนึ่งของการศึกษาตามหลักสูตรปริญญาวิศวกรรมศาสตรดุษฎีบัณฑิต
สาขาวิชาวิศวกรรมโยธา ภาควิชาวิศวกรรมโยธา
คณะวิศวกรรมศาสตร์ จุฬาลงกรณ์มหาวิทยาลัย
ปีการศึกษา 2560

Thesis Title	An Application of Geosynthetic Cementitious Composite Mat for Slope Stabilization
By	Mr. Phong Tan Ngo
Field of Study	Civil Engineering
Thesis Advisor	Professor Suched Likitlersuang, Ph.D.

Accepted by the Faculty of Engineering, Chulalongkorn University in Partial Fulfillment of the Requirements for the Doctoral Degree

.....Dean of the Faculty of Engineering
(Associate Professor Supot Teachavorasinskun, D.Eng.)

THESIS COMMITTEE

.....Chairman
(Associate Professor Supot Teachavorasinskun, D.Eng.)
.....Thesis Advisor
(Professor Suched Likitlersuang, Ph.D.)
.....Examiner
(Associate Professor Tirawat Boonyatee, Ph.D.)
.....Examiner
(Associate Professor Boonchai Ukritchon, Ph.D.)
.....External Examiner
(Professor Akihiro Takahashi, D.Eng.)

ฟง ทาน โง : การประยุกต์ใช้แผ่นซีเมนต์ใยสังเคราะห์คอมโพสิตสำหรับเสถียรภาพของลาดดิน (An Application of Geosynthetic Cementitious Composite Mat for Slope Stabilization) อ.ที่ปรึกษาวิทยานิพนธ์หลัก: สุเชษฐ์ ลิขิตเลอสรวง, 80 หน้า.

ในปัจจุบันมีการพบปัญหาการกัดเซาะและสูญเสียเสถียรภาพของลาดดินจากกระทำของน้ำฝนและการไหลของน้ำใต้ดินโดยเฉพาะบริเวณภูเขา มีงานวิจัยหลายงานที่เน้นไปที่การสร้างเทคโนโลยีใหม่ หรือหาวัสดุใหม่เพื่อเพิ่มเสถียรภาพของลาดดิน ในการศึกษานี้ มีการศึกษาวัสดุใหม่ที่เรียกว่า แผ่นซีเมนต์ใยสังเคราะห์คอมโพสิต เพื่อใช้เสริมกำลังของลาดดิน มีการใช้แบบจำลองเชิงกายภาพร่วมกับวิธีการคำนวณเชิงตัวเลขเพื่อจำลองและศึกษาพฤติกรรมลาดดินทรายที่เสริมกำลังด้วยแผ่นซีเมนต์ใยสังเคราะห์คอมโพสิตภายใต้การไหลของน้ำใต้ดิน มีการใช้เทคโนโลยีภาพถ่ายที่เรียกว่าภาพถ่ายความเร็วของอนุภาค เพื่อวัดการเคลื่อนตัวของดินทรายในแบบจำลองเชิงกายภาพ นอกเหนือไปจากนี้ มีการศึกษาด้วยแบบจำลองหมุนเหวี่ยงที่ใช้ความเร่ง 25 เท่าของความเร่งโน้มถ่วงของโลก แบบจำลองลาดดินที่จำลองภายใต้แบบจำลองหมุนเหวี่ยงสามารถดำเนินการศึกษาได้ทั้งกรณีการไหลของน้ำใต้ดินและภายใต้การกระทำของน้ำฝน สำหรับการจำลองวัสดุแผ่นซีเมนต์คอมโพสิตในแบบจำลองหมุนเหวี่ยง จะถูกแทนที่ด้วยแผ่นพลาสเตอร์ทางการแพทย์ที่มีกำลังและความแข็งใกล้เคียงกัน ในการนี้มีการพัฒนาและติดตั้งแท็งค์น้ำและเครื่องจำลองน้ำฝนสำหรับการทดสอบภายใต้การไหลของน้ำใต้ดินและการกระทำของน้ำฝนตามลำดับ ผลการศึกษาพบว่าแผ่นซีเมนต์คอมโพสิตที่มีความแข็งแรงและแรงเสียดทานระหว่างผิวสัมผัสของแผ่นซีเมนต์คอมโพสิตกับดินทรายสูง สามารถลดการเคลื่อนตัวของลาดดินได้อย่างมีนัยสำคัญ นอกเหนือจากนั้น ด้วยคุณสมบัติการทึบน้ำของแผ่นซีเมนต์คอมโพสิต ยังสามารถลดการซึมผ่านได้ของน้ำฝนลงสู่ดินและชลอการเพิ่มขึ้นของระดับน้ำใต้ดินซึ่งเป็นสาเหตุหลักที่ทำให้เกิดการกัดเซาะและวิบัติของลาดดินได้ ด้วยเหตุผลข้างต้น แผ่นซีเมนต์คอมโพสิตแสดงให้เห็นว่ามีคุณสมบัติที่โดดเด่นในการใช้เพิ่มเสถียรภาพของลาดดินได้

ภาควิชา วิศวกรรมโยธา ลายมือชื่อนิสิต .....

สาขาวิชา วิศวกรรมโยธา ลายมือชื่อ อ.ที่ปรึกษาหลัก .....

ปีการศึกษา 2560

5771480221 : MAJOR CIVIL ENGINEERING
KEYWORDS: PHYSICAL MODELING; CENTRIFUGE MODELING; GEOSYNTHETIC CEMENTITIOUS COMPOSITE MAT; SLOPE STABILITY; RAINFALL; SEEPAGE

PHONG TAN NGO: An Application of Geosynthetic Cementitious Composite Mat for Slope Stabilization. ADVISOR: PROF. SUCHED LIKITLERSUANG, Ph.D., 80 pp.

In recent years, soil erosion and slope instability caused by seepage and rainfall are major problems, especially in the mountain area. Many research studies have focused on finding a new technology or material to stabilize the soil slope. In this study, a novel material called geosynthetic cementitious composite mat (GCCM) is selected to study its performance on soil slope stabilization. A series of 1-g physical model tests and numerical simulation (Plaxis 2D) on sandy soil slopes stabilized with and without GCCM are performed under seepage condition. In addition, centrifuge modeling of soil slopes is performed under 25-g in seepage and rainfall conditions. Particle image velocimetry (PIV) technique is employed to measure the displacement of soil in 1-g physical model tests, whereas accelerometer is used to measure the displacement of soil in 25-g centrifuge model tests. In 25-g centrifuge model test, the GCCM material is modeled using an equivalent strength and stiffness medical gypsum plaster sheet. In-house developed water tank and rainfall simulator are calibrated to simulate the seepage and rainfall. The results show that the GCCM can reduce the displacement of the slope by its high stiffness and interface friction. Additionally, the GCCM can delay the increase of water pressure raising that leads to diminishing the hydraulic force acting on the soil slope. The result indicates that the GCCM shows a good performance in slope stabilization.

Department:	Civil Engineering	Student's Signature	.....
Field of Study:	Civil Engineering	Advisor's Signature	.....
Academic Year:	2017		

ACKNOWLEDGEMENTS

First of all, I would like to express my profound gratitude to my supervisor, Professor Suched Liketlersuang, for his enthusiastic guidance, extraordinary support, and effectual encouragement throughout this research. I would like to express my deepest gratitude to my co-supervisor, Professor Akihiro Takahashi, for his giving helpful advice, productive suggestions and discussions. All help I receive from my supervisor and co-supervisor are gratefully acknowledged and will never be forgotten.

I would like to extend my gratitude to Associate Professor Boonchai Ukritchon, Associate Professor Supot Teachavorasinskun, and Associate Professor Tirawat Boonyatee for giving useful comments on my dissertation, serving and sharing their time on my dissertation defense committee.

I acknowledge my gratitude to Mr. Bhakapong Bhadrakom and Dr. Krisada Chaiyasarn for their recommendation on using Particle Image Velocimetry method to measure the displacement of soil as well as how to get a good frame for PIV analysis. I owe a debt of gratitude to Mr. Sakae Seki and Mr. Yuthakarn Suwanawate who helped me to carry out my experiments.

I would like to extend my sincere gratitude to AUN/SEED.Net for funding me during my study on the Ph.D. sandwich program at Chulalongkorn University and Tokyo Institute of Technology.

I would like to take this opportunity moment to show my deepest gratitude to my parents, my parents-in-law, my brothers and young sister for their love, support, and continued encouragement. I also wish to express my special thanks to my beloved wife whose patience, sufferance and love are invaluable. Thanks to my beloved daughters Phuong Minh, Phuong Dinh, and Xuan Nguyen who offer me a constant source of motivation.

Finally, I would like to show my sincere gratitude to all my friends at Chulalongkorn Universiy, TokyoTech, and especially at Rajatevee building for their help, warm friendship, and encouragement.

CONTENTS

Page

Page

Chapter 1: Introduction

1.1 Background

Landslide is a geological phenomenon related to ground movements such as rock-falls, deep or shallow failure of slope. Landslide seriously destroys properties and human life (Intarawichian and Dasananda, 2011). Recent years, there were many landslide hazards happening over the world, especially in Thailand. The North and South of Thailand are the areas where landslide hazard is a serious problem (Soralump, 2010).

Landslide often occurs at places such as hill, highland, and mountain areas (Fowze et al., 2012) where the slopes are almost structured by residual soil covering over bedrock. Since typical characteristics of the residual soil are high permeability, low compression, low shear strength, easily reduced strength when wetting caused by rainfall, those properties are not advantaged for slope stability and erosion resistance.

Stability of slope depends on the primary driving force caused by gravity force acting on the soil mass and other factors such as geological condition, terrain, structure of slope, soil properties, groundwater level, vegetation, and rainfall condition. Rainfall is one of the most important factors affecting the stability of slope. During the last decade, in Thailand, so many landslides happened due to heavy rainfall (Khamfong et al., 2013; Soralump, 2010). It should be noted that shallow landslides, e.g., 1-2m depth, are common type induced by rainfall (Ng et al., 2015; Ono et al., 2014).

Climate change has great impacts on weather conditions, especially to heavy rainfall (Donat et al., 2016; Lehmann et al., 2015). Recent investigations show that heavy rainfall tends to exacerbate geo-disasters (Chen et al., 2006; Fuchu et al., 1999; Guzzetti et al., 2004; Peng et al., 2015; Yasuhara et al., 2012). In Thailand, every 3 to 5 years large landslide triggered by heavy rainfall occurs, and the frequency of rain-triggered landslide has increased (Fowze et al., 2012; Soralump, 2010). For example, on May 23, 2006, a large landslide occurred in northern Thailand destroyed about 4,000 houses and more than 10,000 people had evacuated (Boonyanuphap, 2013). Landslide is, therefore, a serious problem to human beings.

1.2 Statement of problem

Rainwater infiltrates into natural slope composed of residual soil and makes pore-water pressure as well as temporary water level increase. The pore-water pressure plays an important role in the stability of slope (Rahardjo et al., 2008), and the increase of pore-water pressure makes the stability of slope toward to be unstable. In addition to slope stability, rainwater also causes the process of soil erosion to be more serious.

There are many methods available for reinforcing natural slope: reducing the slope angle; nail and/or anchor combined with shotcrete, geotextile, geosynthetic clay liner, wooden pile, concrete pile; gabion; vegetation approach such as live stakes and vetiver grass, etc. Each method mentioned previously always has specific advantages and limitations. The limitations, in general, can be listed as follows: (1) much time needed for construction, (2) high cost of construction, (3) maintenance regularly, (4) and not friendly to the environment. Balancing advantages and limitations is, therefore, still a problem on which we should focus.

Recently, some materials such as geosynthetics clay liner, concrete canvas, and concrete clothes have been used to reinforce natural slopes subjected to heavy rainfall and seepage, but it probably seems to be still not enough. In this study, a novel material called geosynthetic cementitious composite mat (GCCM) used to reinforce sandy slope under seepage and heavy rainfall is investigated.

1.3 Objective

The objective of this study is to investigate the deformation characteristics and stability of soil slope reinforced with geosynthetic cementitious composite mat.

The objective could be divided into sub-objectives as follows:

1) To determine the physical and mechanical properties of GCCM;
2) To determine the mechanical interaction between GCCM and soil;
3) To perform soil slope models using 1-g physical modeling and 25-g centrifuge modeling;
4) To monitor the displacement of soil slope using digital image analysis;
5) To simulate slope reinforced with GCCM using PLAXIS 2D.

1.4 Scopes

In order to achieve the aforementioned objective, the following scopes have to be done:

1) Conducting a series of laboratory tests to determine the engineering properties of materials;
2) Developing a 2D plane strain tank for soil slope model;
3) Calibrating for PIV technique to measure the deformation of slope;
4) Performing 1-g physical model tests under seepage condition and doing numerical simulation;
5) Performing 25-g centrifuge model tests under seepage and rainfall conditions.

1.5 Expected outcome

The expected outcome is to propose a novel material called geosynthetic cementitious composite mat for slope stabilization and soil erosion control.

1.6 Dissertation structure

The structure of this dissertation consists of seven chapters. The contents of each chapter are summarized as follows.

Chapter 1: This chapter introduces the background and the statement of problem related to the present study. Based on this, the objective and scopes are established. Additionally, the expected outcome and the dissertation's structure are also stated out.

Chapter 2: This chapter shows the literature review. Many research studies related to geosynthetic materials, shallow slope failure, techniques for reinforcing slope, physical modeling, centrifuge modeling, and PIV technique are summarized and discussed. The reason for doing research on using a geosynthetic cementitious composite mat (GCCM) for slope stabilization is pointed out in this chapter as well.

Chapter 3: This chapter focuses deeply on GCCM's composition and its physical and mechanical properties.

Chapter 4: Methodology of testing models is presented in this chapter. Two kinds of models are set up. The first one is the 1-g physical model, the second one is

the 25-g centrifuge model. Details of the model tests such as materials, equipment, slope model, and experimental program are also described in this section.

Chapter 5: Results of the 1-g physical model tests are shown and discussed in this section. Two principal parts focused on in this chapter are the change of pore water pressure within slope and the displacement of soil slope under seepage. In addition, numerical simulation (Plaxis 2D) of slope reinforce with/without GCCM is also provided.

Chapter 6: Results of the 25-g centrifuge model tests are shown and discussed in this section. Two principal parts focused on in this chapter are the change of pore water pressure within slope and the displacement of soil slope under seepage and rainfall.

Chapter 7: Finally, the conclusion and recommendation are drawn in this section.

Chapter 2: Literature review

Geosynthetic is a planar product made from polymeric materials. There are common types of geosynthetic such as geotextile, geogrid, geonet, geomembrane, geopipe, geofoam, and geocomposite. Over the past two decades, geosynthetics have been used in a wide range of applications such as transportation, geotechnics, environment, and hydraulics. Geosynthetic products are still being developed for other private applications.

Geosynthetic clay liners (GCLs), for example, have been developed to replace compacted clay liners in cover systems and bottom liners of waste containment. GCLs are comprised of a thin layer of bentonite bonded to layers of geosynthetic. Because their hydraulic conductivity to water is very low, GCLs are also used as environmental protection barrier in roads, storage tanks, or as single liners for canals or ponds. The main advantages of the GCL are the limited thickness, good compliance with differential settlements of underlying soil or waste, easy installation, and low cost (Bouazza, 2002). The use of GCL is mostly in liners for landfill and mining applications (Rowe, 2014). However, the low strength of hydrated bentonite may not be effectively used for soil reinforcement, and it can produce vulnerability to mechanical accidents.

A new composite material called textile reinforced concrete (TRC) has been developed in many manners (Colombo et al., 2013; Hegger and Voss, 2008; Tsesarsky et al., 2013). In general, textile layers are introduced to improve the tensile strength of concrete. However, the strength, ductility properties and drying shrinkage of TRC depend significantly on its components and bonding between textile and cement layers (Fangyu et al., 2014; Fangyu et al., 2015; Han et al., 2014; Zhang et al., 2017). Recently, concrete canvas, which is the product invented by Brewin and Crawford in 2005 in the UK, has been commercially launched (Concrete_Canvas_Ltd.). This is an idea of using cement impregnated fabric as a new construction material. It is used to replace conventional concrete (in-situ, precast or sprayed) for erosion control, remediation, and construction applications. Some typical applications are ditch lining for drainage and

irrigation, surface erosion control for slope protection, and remediation of cracked and damaged concrete infrastructures.

Shallow slope failure is a geotechnical phenomenon related to the movement of soil at a shallow depth less than 1 m – 2 m (Evans, 1972). Shallow slope failure does not cause major damage or loss of human life, but it can constitute a hazard to infrastructure by causing damage to the guardrail, shoulders, road surface, drainage facilities or impacting public traffic because of debris flow onto road pavement (Titi and Helwany, 2007). Shallow slope failure usually occurs in the rainy season. Seepage developing parallel to the slope surface due to rainfall is one of the main reasons that cause the slope instability (Day and Axten, 1989).

Many studies on the stability of slope under seepage flow have been conducted using physical model tests. By measuring pore water pressure, moisture content, and slope deformation in a sandy slope subjected to water percolation from the upslope, Orense et al. (2004) found that slope failure was always induced when the soil near the toe of slope reached nearly full saturation condition. This finding was also supported by observations made by Huang et al. (2009). In addition, some research has focused on the development of new material using geosynthetics for slope stabilization. Applications of geosynthetics on geotechnical engineering problems have been increasing rapidly (Koerner 2012). There were many products of geosynthetics been studied and developed in particular that applied to stabilize the earth slope and the embankments on soft soil (Akay et al. 2013; Bergado et al. 2002; Chen et al. 2012; Da Silva et al. 2017; Tavakoli Mehrjardi et al. 2016; Thuo et al. 2015; Zhang et al. 2015). Almost three decades ago, applications of geotextile (Fowler and Koerner, 1987) and geocell (Bush et al., 1990) for embankment construction on soft soil were studied. Later years, many materials made from geosynthetic were developed and applied for slope stabilization and land reclamation such as three-dimensional polyethylene geocells (Wu and Austin, 1992), heavy duty polyester woven geotextile (Raymond et al., 1993), geosynthetic mulching mat (Ahn et al., 2002), slurry filled geotextile mats (Yan and Chu, 2010). In addition, the geosynthetic reinforced soil slopes subjected to earthquake loads were studied by Thusyanthan et al. (2007) and Wang et al. (2011). For seepage flow causing slope failure, centrifuge model studies on fine sandy slopes under seepage

condition to evaluate the performance of anchored geosynthetic systems on the slope stability were carried out by Rajabian et al. (2012), Rajabian and Viswanadham (2016). Akay et al. (2013) introduced a lightweight material called expanded polystyrene geofoam for slope remediation undergoing seepage flow.

In order to stabilize slope from shallow failure, various techniques have been used such as vegetation (Wu, 1994), live poles (Mafian et al., 2009; Wu et al., 2014), shotcrete (US-Army-Corps-of-Engineers, 1995), geosynthetic clay liners (GCLs) (Daniel et al., 1998; Gilbert and Wright, 2010). Each technique mentioned above has specific limitations. For example, vegetation and live pole need time to grow up and maintain regularly; for shotcrete technique, quality and thickness of the concrete cover are not uniform; for GCLs, the leaking of clay out of GCLs sheet that would reduce the friction between GCLs and soil slope (Bouazza, 2002). Therefore, there is a need for studies to investigate a new material that would not only reinforce slope but also satisfy these limitations aforementioned. Geosynthetic cementitious composite mat (GCCM) is, for instance, one of such new materials (Jongvivatsakul et al., 2018). An idea to improve the performance of GCL on strength and stiffness by replacing bentonite with cement leads to develop a novel material named geosynthetic cementitious composite mat. GCCM can provide a hard-wearing erosion control surface for protecting slopes and can delay infiltration rates of rainfall causing slope instability. The GCCM product is designed for civil engineering applications particularly for geotechnical engineering problems such as slope stabilization, erosion control, ditch lining, and contamination. GCCM may probably be used as an alternative to shotcrete to protect slopes where vegetation technique is unsuitable due to high flow rates, arid climate, or poor soil conditions. As for composition, GCCM is a hybrid material comprised of two layers of geotextile and a dry cement layer. The cement layer is bounded between two geotextile layers using needle punching. During installation, the water spraying is required to hydrate the GCCM for a couple days. Then GCCM becomes harden like a solid mat with high tensile and bending strength.

To study the performance of the reinforced slope, measurement of slope deformation is crucial. There are various image-based analysis techniques have been used to measure planar deformation of soil in geotechnical tests such as X-ray (Arthur

et al., 1964; Roscoe et al., 1963), stereo-photogrammetric techniques (Andrawes and Butterfield, 1973; Butterfield et al., 1970), and particle image velocimetry (PIV) (Paikowsky and Xi, 2000; Taylor et al., 1998; White et al., 2003). Among them, PIV is a well-known technique used to measure velocity in fluid dynamics (Adrian, 1991). It allows obtaining instantaneous velocity measurements and related properties at a specific area, called interrogation areas, in the fluid. PIV technique has its roots from Laser Speckle Velocimetry technique developed in the late 1970s (Dainty, 1975). In PIV, the displacement of an interrogation area of a pair of digital images is calculated with help of cross-correlation or autocorrelation techniques. In the present study, the PIV technique is employed to predict the deformation of soil slope because it is simple, cheap, and no need to make target markers within the soil.

Geotechnical centrifuge modeling is a technique for testing a physical model of geotechnical engineering problems related to the bearing capacity of the foundation, retaining wall, embankment, slope, tunnel, etc. (Madabhushi, 2014). The purpose of this technique is to provide stresses in the model as same as the stresses in the prototype by spinning the model to increase the acceleration (N-g) acting on the model. According to Rajabian et al. (2012), stress-strain characteristics in the field cannot be reproduced in the small-scale physical model because the stresses in the physical model are comparatively low. Therefore, the centrifuge modeling can be considered as a good choice to model geotechnical problems. Many centrifuge modelling slopes reinforced with geotextile, geogrid, and anchored geosynthetic system have been carried out under seepage, differential settlement, earthquake, and drawdown (Hu et al., 2010; Luo et al., 2018; Raisinghani and Viswanadham, 2011; Rajabian et al., 2012; Sharma and Bolton, 1996; Viswanadham and König, 2009; Wang et al., 2011). However, research related to using GCCM to reinforce slope in the geotechnical centrifuge cannot be found.

Based on the literature review shown above, it can be seen that research studies on GCCM and its application in slope stability are limited. This study focuses on the GCCM's properties and on the use of GCCM to reinforce slope under seepage and rainfall through conducting 1-g physical model tests and 25-g centrifuge model tests.

Chapter 3: Geosynthetic cementitious composite mat (GCCM)

The idea of GCCM material comes from a material called Geosynthetic Clay Liner (GCL), which had been developed and used since 1988 in the United States and Germany. The engineering function of a GCL is containment as a hydraulic barrier to water, leachate, or other liquids and sometimes gases. GCL is comprised of a thin layer of sodium or calcium bentonite bonded to layers of geosynthetic such as geotextile or geomembrane (Bouazza, 2002). The GCCM product studied here is similar to GCL except for the middle layer of bentonite is replaced by fiber-cement powder layer.

In this chapter, GCCM's composition and its properties such as mass per unit area, nominal thickness, water impermeability, tensile strength, bending strength, puncture test, and interface friction angle are studied.

3.1 GCCM's composition

Geosynthetic cementitious composite mat is a novel material comprised of three layers, which are a non-woven geotextile on the top, a fiber-cement powder layer in the middle, and a woven geotextile at the bottom, as shown in Fig. 3-1. GCCM is formed into rolls with a thickness of 10 mm, a width of 1 m, and the length of GCCM up to 30 m. Since the product is manufactured in the factory, the properties of GCCM are uniform compared to other products that installed in the field, e.g., shotcrete. After spraying water on GCCM's surface for a certain curing time, the cement within GCCM is hydrated, so GCCM becomes a solid material with high stiffness and tensile strength. In addition, the combination of cement layer and the two geotextile layers at the top and bottom make GCCM can absorb a large strain caused by the external load during operation. Moreover, the construction and installation of GCCM for slope stabilization are simple and quick, e.g., only laying GCCM on the surface of slope and then spraying water on GCCM.

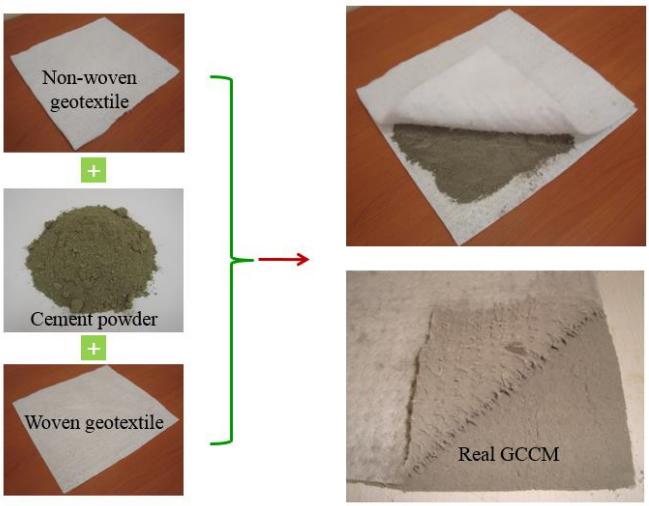

(a) Composition of GCCM

(b) Manufacturing process of GCCM

Fig. 3-1 Composition and manufacturing process of GCCM

3.2 GCCM's potential applications

It can be expected that the potential applications of GCCM in geotechnical problems are plenty and wide, for example, such as slope stabilization, erosion control, ditch lining, containment as a hydraulic barrier to water, and other purposes in rural areas, etc.

3.3 GCCM's properties

Basic physical and mechanical properties of GCCM determined in this section are mass per unit area (ASTM-D5993 2014), nominal thickness (ASTM-D5199 2006), tensile

strength (ASTM-D6768 2006), bending strength (BS-EN-12467 2012), puncture resistance (ISO-12236 2013), water impermeability (BS-EN-12467 2012), and interface friction angle (ASTM-D3080-98, 1998). Table 3-1 shows a list of standards that are adopted to determine the physical and mechanical properties of GCCM.

Table 3-1 List of standards used in GCCM's tests

Standard	Title
ASTM-D5993 (2014)	Standard Test Method for Measuring Mass Per Unit of Geosynthetic Clay Liners
ASTM-D5199 (2006)	Standard Test Method for Measuring the Nominal Thickness of Geosynthetics
ASTM-D6768 (2006)	Standard Test Method for Tensile Strength of Geosynthetic Clay Liners
BS-EN-12467 (2012)	Fibre-cement flat sheets - Product specification and test methods
ISO-12236 (2013)	Geosynthetic static puncture test
BS-EN-12467 (2012)	Fibre-cement flat sheets - Product specification and test methods
ASTM-D3080-98 (1998)	Standard Test Method for Direct Shear Test of Soils Under Consolidated Drained Conditions

3.3.1 Real water absorbed by cement in GCCM

Real absorbed water is defined as the real water absorbed by cement powder in the middle layer of GCCM when water sprayed into GCCM. Real absorbed water is always less than the amount of sprayed water because of the geotextiles available.

During installation, the GCCM must be hydrated by spraying with water. Spaying water on the non-woven geotextile surface for several minutes is recommended. A ratio of water per GCCM and a setting time are two important factors that affect the physical properties of the GCCM during installation. The ratio of water per GCCM (w/W_{GCCM}) is defined by the weight of water per the total dry weight of the

GCCM. To simulate the installation condition, the water absorption test is firstly carried out to define the w/W_{GCCM} at the saturated condition. The water is sprayed on the GCCM at 0.25, 0.50, 0.75 and 1, respectively. To determine the water per cement ratio (w_a/c), the dried GCCM's specimens of 10 cm × 10 cm are firstly prepared and weighted. Then, the water is sprayed on the GCCMs and wait for a few minutes, e.g., 5 min, to ensure that all the water is absorbed. It should be noted that since the standard for determining water absorption of GCCM is not available, duration of 5 min chosen also aims to perform this test as fast as possibly to limit the hydration of cement within GCCM. The soaked GCCMs are weighted. Both non-woven and woven geotextiles are gently taken off in the container. The cement paste and wet geotextiles are weighted. Some cement paste may still remain within the geotextiles. After that, all components are oven-dried at 110°C for 24 hours and weighted. After oven drying, the cement paste remaining within the geotextiles are simply removed. The ratio of w_a/c is defined by:

$$w_a/c = \frac{\text{weight of water absorption by cement}}{\text{weight of cement powder}} \qquad (3\text{-}1)$$

Where,

+ The weight of water absorption by cement = the weight of soaked GCCM – the weight of wet geotextiles – the weight of cement powder

+ The weight of cement powder = the weight of dried GCCM – the weight of oven-dried geotextiles. It is noted that at least three replicates are performed for each ratio of w_a/c

The results from the water absorption test can construct a plot between w_a/c and w/W_{GCCM} as presented in Fig. 3-2. The result shows that when spraying the water more than w/W_{GCCM} = 0.5 the leftover water will flow out from the specimen. This can be concluded that the saturated water is w/W_{GCCM} = 0.5 which associated with w_a/c of 0.3. Therefore, the testing specimens are prepared according to the saturated condition of water.

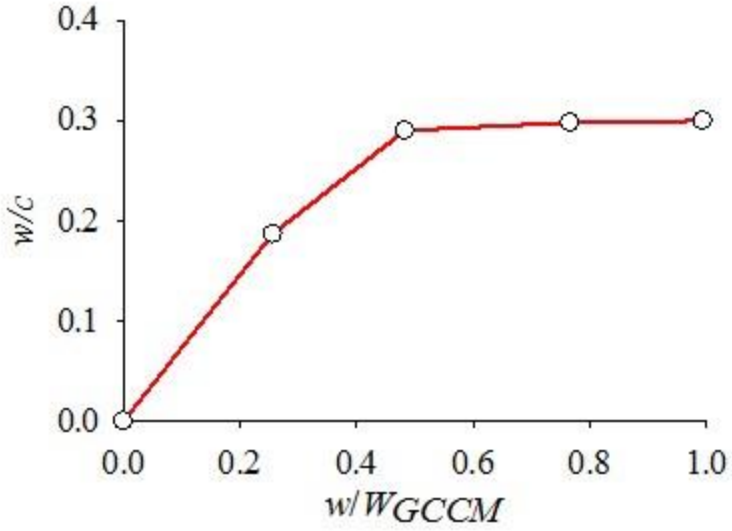

Fig. 3-2 Relationship between the water per cement ratio (W_a/C) and the ratio of water per GCCM (w/W_{GCCM}) from the water absorption tests

3.3.2 Mass per unit area

Standard ASTM D5993 is employed to test mass per unit area of GCCM as well as geotextile of which GCCM is made.

For geotextile, the results show that the values of mass per unit area of non-woven and woven geotextile are 279 g/m^2 and 168 g/m^2, respectively. These values are consistent with the typical values of ≥ 220 g/m^2 and ≥ 110 g/m^2, which are provided by Ceteau-LTD. (2014). Table 3-2 describes more details.

Table 3-2 Mass per unit area of non-woven and woven geotextile

Type	Non-woven	Woven
Length, mm	461	263
Width, mm	501	358
Weight, g	64.41	15.81
Mass per unit area, g/m^2	279	168

For GCCM, the results show that the mass per unit area of GCCM increases by curing time, and it tends to be stable after 3-day curing time. The values of mass per unit area after 1, 3, and 7 days are 1.12 g/cm^2, 1.34 g/cm^2, and 1.35 g/cm^2, respectively, as presented in Table 3-3. In order to be visible, the change of mass per unit area vs.

curing time is plotted in Fig. 3-3. It should be noted that the ratio of $w/W_{GCCM} = 0.5$, and specimens are soaked.

Table 3-3 Mass per unit area of GCCM after specimens cured for 1, 3, and 7 days

Curing time (day)	Average length (mm)	Average width (mm)	Mass (g)	Mass per unit area (g/cm^2)
1	11.0	10.7	129.45	1.12
3	11.0	10.7	155.76	1.34
7	11.0	10.7	158.99	1.35

Remark: Number of specimens is five, and $w/W_{GCCM} = 0.5$

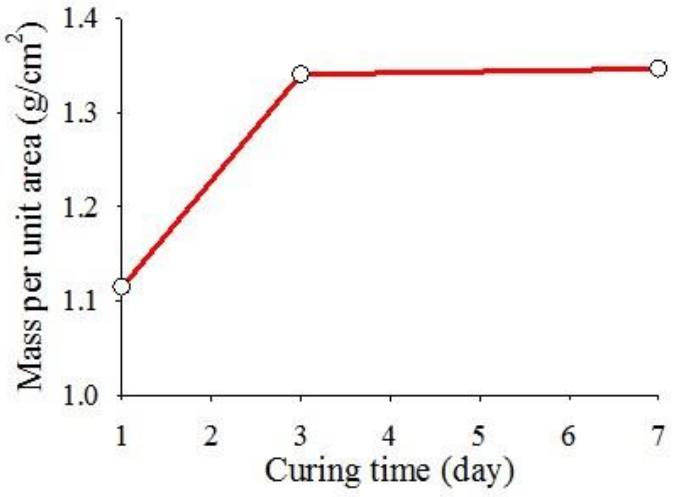

Fig. 3-3 Mass per unit area of GCCM vs. curing time

3.3.3 Nominal thickness

Standard ASTM D5199 is employed to test the nominal thickness of GCCM as well as geotextile of which GCCM is made.

For geotextile, the results show that the nominal thicknesses of non-woven and woven geotextile are 3.86 mm and 0.49 mm as shown in Table 3-4.

Table 3-4 Nominal thickness of non-woven and woven geotextile

	Non-woven	Woven
Average nominal thickness (mm)	3.86	0.49

For GCCM, the results show that nominal thickness of GCCM does not change significantly after 1, 3, and 7 days of curing time. The average value of nominal thickness is 8.09 mm as seen in Table 3-5 and Fig. 3-4.

Table 3-5 Nominal thickness of GCCM

Curing time (day)	Average nominal thickness (mm)	Number of specimens
1	8.08	5
3	8.09	5
7	8.09	5

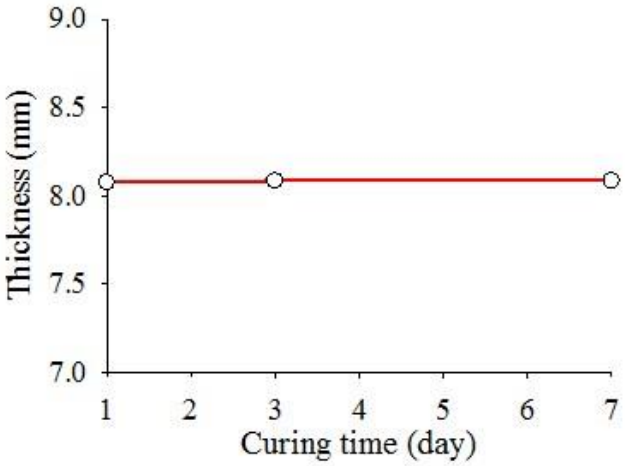

Fig. 3-4 Nominal thickness of GCCM vs. curing time

3.3.4 Water impermeability test

The water impermeability of the GCCM is obtained by testing specimens in a water impermeability tester as shown in Fig. 3-5. The water impermeability is conducted following BS EN 12467. Before the test, GCCM specimens are sprayed with water, e.g., $w/W_{GCCM} = 0.5$, and cured for 7 days. During the test, the test specimen size of 550 mm × 450 mm is soaked under 20-mm height water for 24 hours. Three replicates are tested, and the average values of the flow rate and the hydraulic conductivity are 0.00174 cm^3/s and 7.03×10^{-7} cm/s, respectively. The result exhibits that the GCCM is almost impermeable.

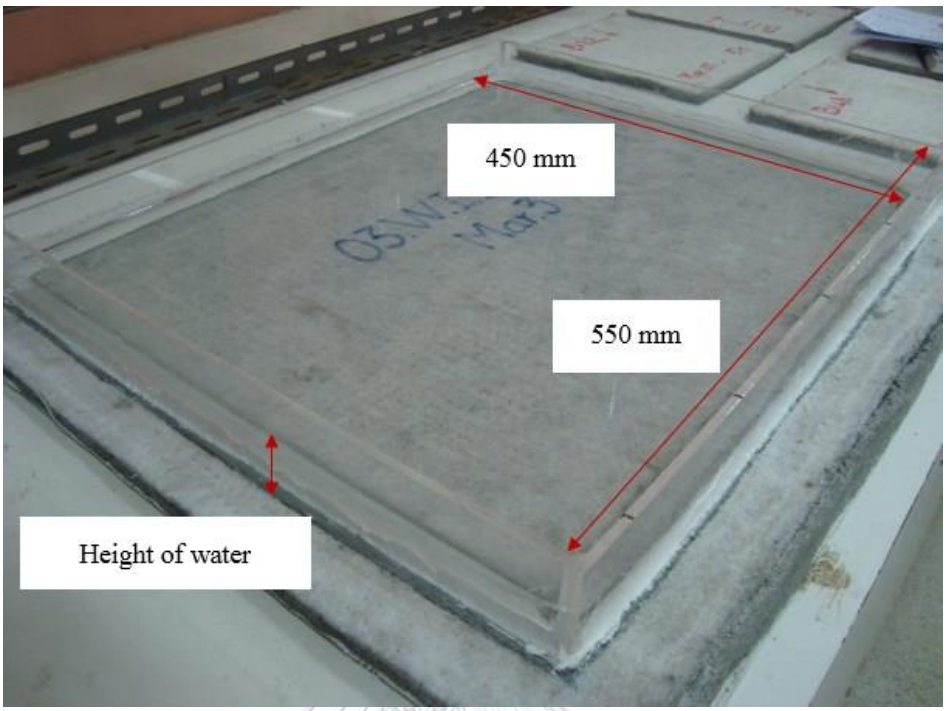

Fig. 3-5 Water impermeability test setup

3.3.5 Tensile strength

The sewing process during manufacturing GCCM might lead to a difference of tensile strength of GCCM along weft (width) direction and wrap (length) direction, so the direct tensile tests are performed for both length and width directions following the ASTM D6768. Fig. 3-6 presents the geometry of tensile specimen and test set up. Specimens are subjected to uniaxial tensile load with the loading rate of 10 mm/min. Four different curing ages (1, 3, 7 and 28 days) of specimens are prepared for the test. Stress-strain curves of specimens with different curing ages are plotted in Fig. 3-7(a). The curves exhibit linear relationship at the beginning and then the curves lightly become non-linear before reaching the first peak stress. After this stage, the load drop because the matrix cracked. Beyond this point, geotextiles take an important role to resist the load until the second peak which is the highest tensile stress. The results show that the differences of stress-strain characteristic between length and width directions are observed. In length direction, the geotextile slips from cement paste after the peak load. This made the reduction of stress in the stress-strain curve after the peak. On the other hand, the peak occurs at higher strain for width direction.

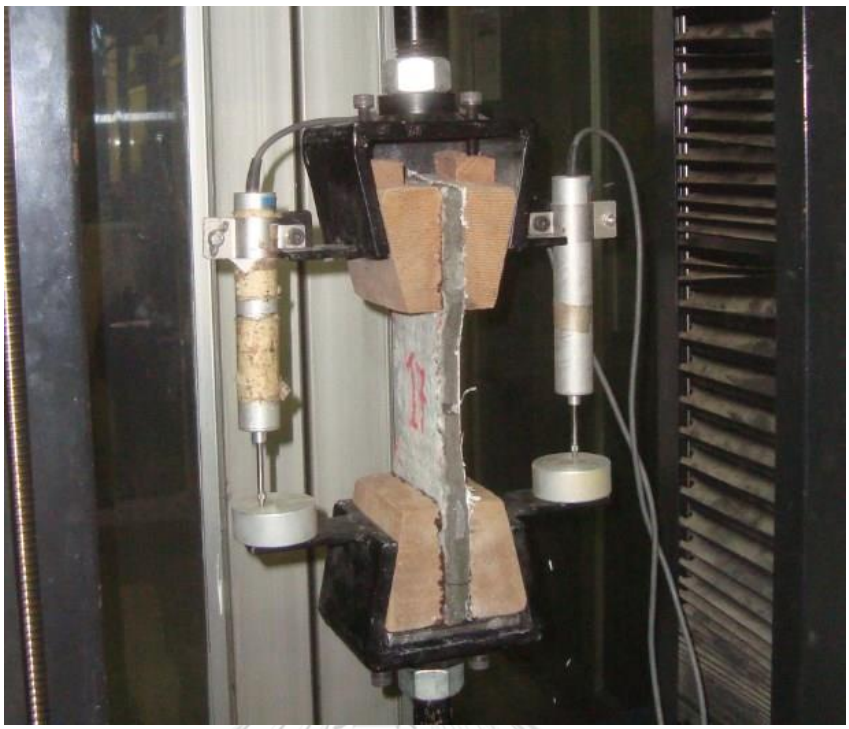

Fig. 3-6 Geometry of specimen and tensile test set up

Tensile strength and Young's modulus averaged from five replicates for each curing age are presented in Fig. 3-7(b) and 3-7(c), respectively. Tensile strength is calculated from the highest tensile load divided by the cross-sectional area of GCCM while Young's modulus is computed from the initial slope of stress-strain curves where the linear behavior is observed. The results show that tensile strength and Young's modulus increase with the increase in curing time. This is because the strength of cement paste developed with time. In addition, the GCCM in width direction provides approximately 48% higher tensile strength and 65% higher modulus than length direction. Since the mechanical properties of woven geotextile are not much different between the weft and warp directions, e.g., tensile strengths are 72.05 MPa and 71.70 MPa in the weft and warp directions, the difference in tensile strength of GCCM might be from the effect of the sewing process. After 7 days of curing, the tensile strengths of GCCM are 2.70 MPa and 2.02 MPa for the width and length directions, respectively. Young's modulus of width direction at 7 days is 352.4 MPa while the modulus of length direction is 240.8 MPa. It is found that tensile strength of GCCM is relatively higher than those of concrete canvas reinforced by 3D spacer fabric (Han et al., 2014).

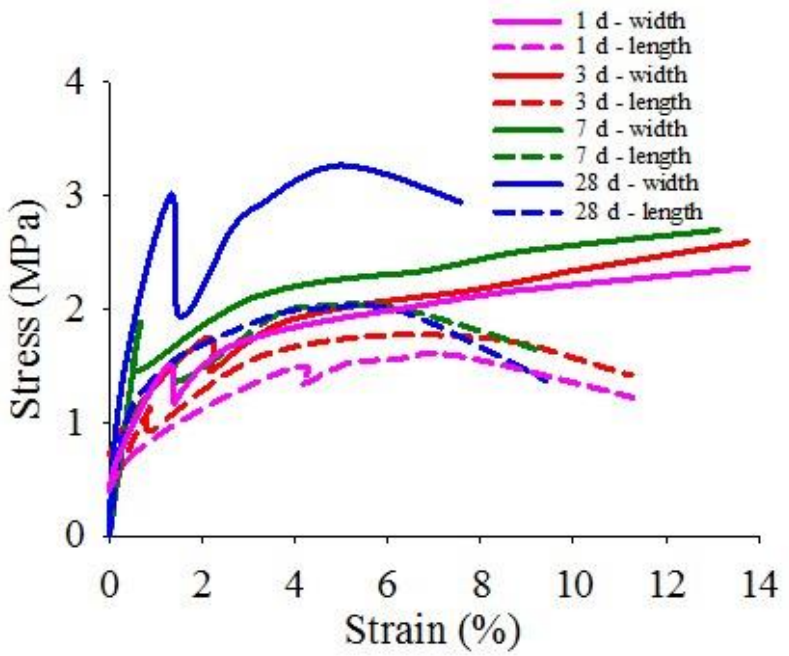

(a) Stress-strain curves

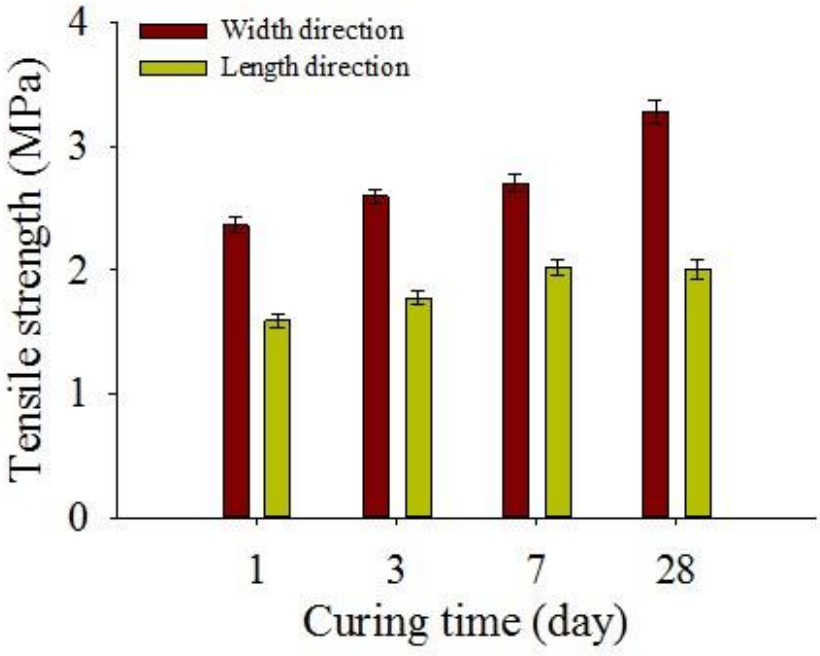

(b) Tensile strength

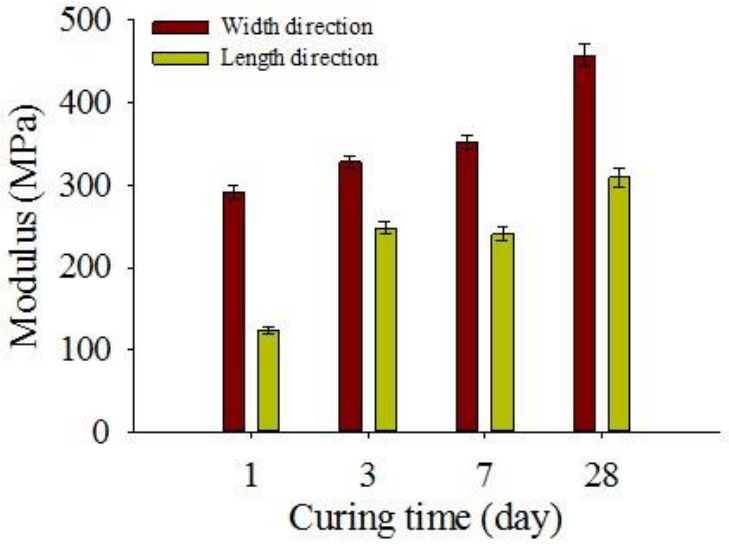

(c) Change of modulus by curing ages

Fig. 3-7 Results of the tensile test

3.3.6 Bending strength

Because the GCCM is expected to resist the bearing load coming from hollow parts on slope surface, foot traffic, or vehicles during the slope protection which may cause the bending stress, the 250 × 250 mm specimens are tested under three-point bending as shown in Fig. 3-8. Displacement transducer is used for measuring mid-span deflection. Load with the loading rate of 10 mm/min is applied until the mid-span deflection reached 40 mm. Similar to the tensile strength test, four different curing ages (1, 3, 7, and 28 days) of specimens are prepared for the bending test. Results of bending test are presented in Fig. 3-9. Bending load-deflection curves (Fig. 3-9(a)) consist of two stages. The first stage presents a composite behavior between geotextiles and cement paste. The curves exhibit the linear relationship until the first peak. At the end of the stage, cement paste is cracked resulting in sudden reduction of load. In the second stage, the geotextiles govern the behavior. Bending load is recovered and tends to increase with the increase in deflection. The bending strength can be calculated by:

$$\sigma_b = \frac{3PL}{2bd^2} \qquad (3\text{-}2)$$

Where P is the maximum load, L is the span of the simple support, b is the width of the specimen and d is the thickness of the specimen. It should be noted that the

change of specimen's cross-sectional area is assumed to be not significant during the test.

In general, the GCCM shows ductile behavior under bending test. Fig. 3-9(b) shows maximum bending stresses, which are determined from five replicated specimens. The standard errors are in the range of 0.03 – 0.43 MPa. Similar to tensile strength, the bending strength increases with curing time. As shown in Fig. 3-1(b), the warp and weft directions in woven geotextile are associated with the length and width directions of the GCCM, respectively. The bending test results also exhibit the significant differences between the length and width directions. In general, the bending strengths along the width direction are 1.5 – 2 times higher than the bending strengths along the length direction.

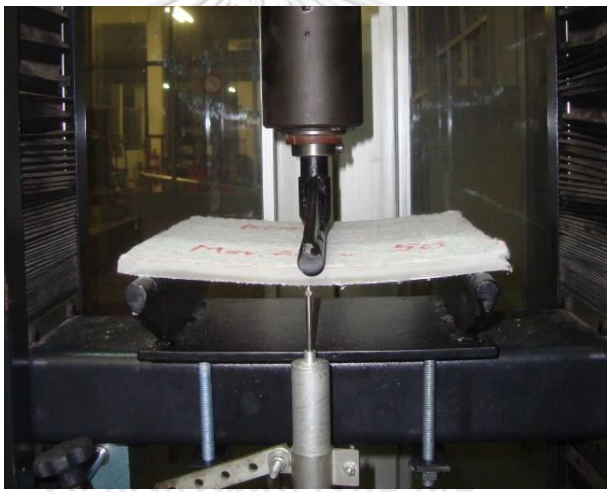

(a) Test setup

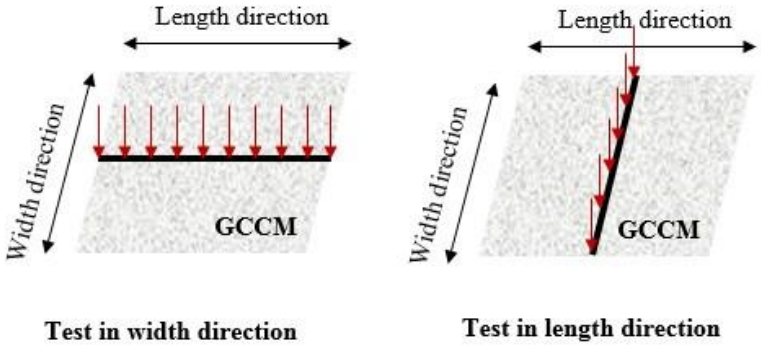

(b) Schematic of bending test in width and length direction

Fig. 3-8 Bending strength test

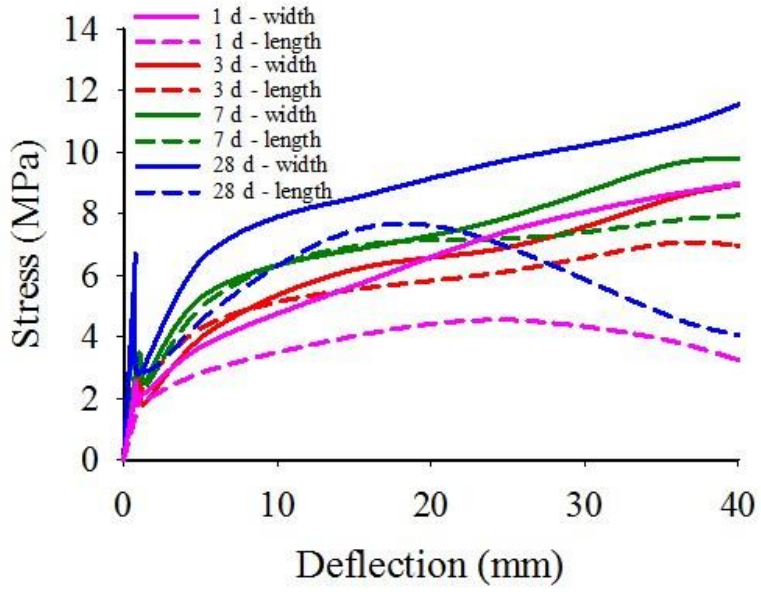

(a) Stress vs. deflection curves of specimens cured for 1, 3, 7, and 28 days

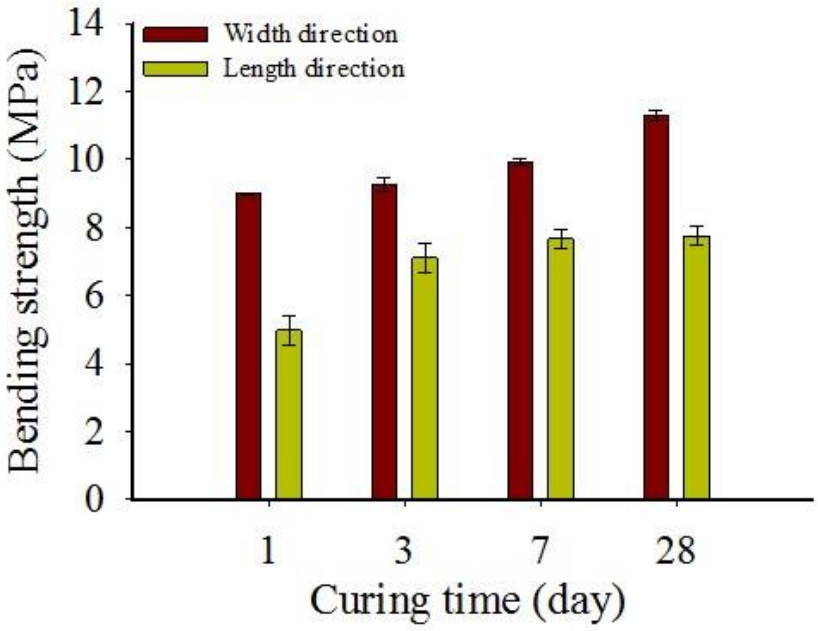

(b) Change of bending strength by curing time

Fig. 3-9 Bending test

3.3.7 Puncture test

Puncture tests are conducted according to ISO standard as demonstrated in Fig. 3-10. A 250 × 250 mm GCCM is clamped between two steel rings and a flat-ended plunger with a diameter of 50 mm was pushed at a constant rate (5 mm/min) of loading on the center of the specimen. The puncture resistance is determined by measuring the force

required to push a plunger through the specimen. The penetration is measured by using displacement transducer during the test. Four different curing ages (1, 3, 7 and 28 days) of specimens are tested. Three replicates are tested for each curing age. Load-penetration relationship is presented in Fig. 3-11(a). The loads at a turning point at small deformation are governed by the matrix and thus influenced by the curing ages. Next, the loads increase with the increase in penetration and reach the peak when the penetration is approximately 20-25 mm. After the peak load, the geotextiles start to rupture and the plunger completely passes through the specimens in final. According to the results in Fig. 3-11(b), the curing time seems not to affect the puncher resistance. This indicates that the maximum puncture load is mainly resisted by geotextiles. Maximum load is varied between 1.60 to 1.72 kN. In contrast with the tensile strength and bending strength tests, the resistance measured from the puncture tests cannot show the differences between the width and length directions due to the axis-symmetry condition of the test mechanism.

Fig. 3-10 Puncture test setup

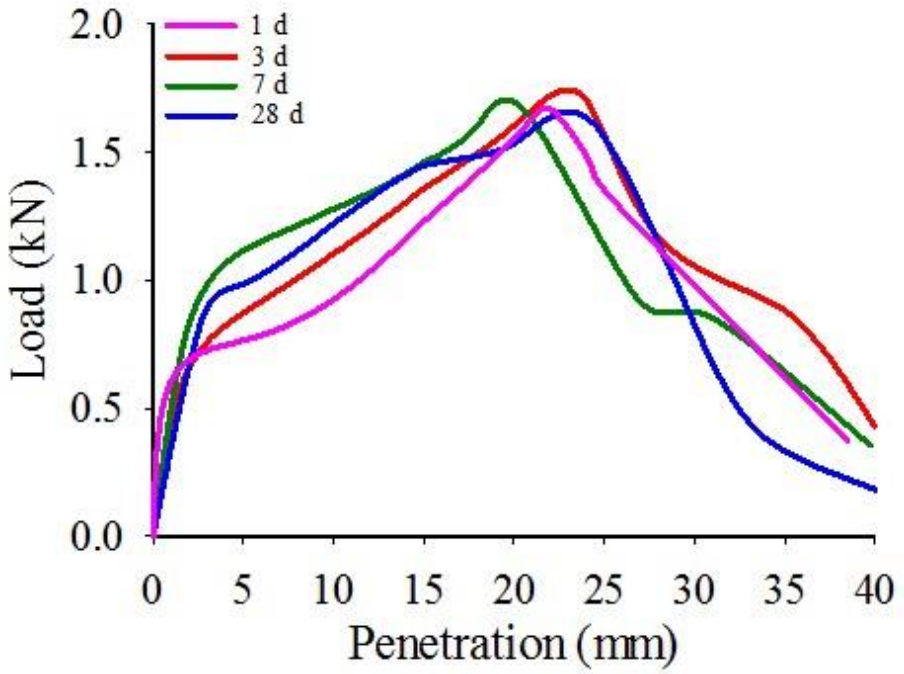

(a) Puncture load vs. penetration curves of specimens cured for 1, 3, 7, and 28 days

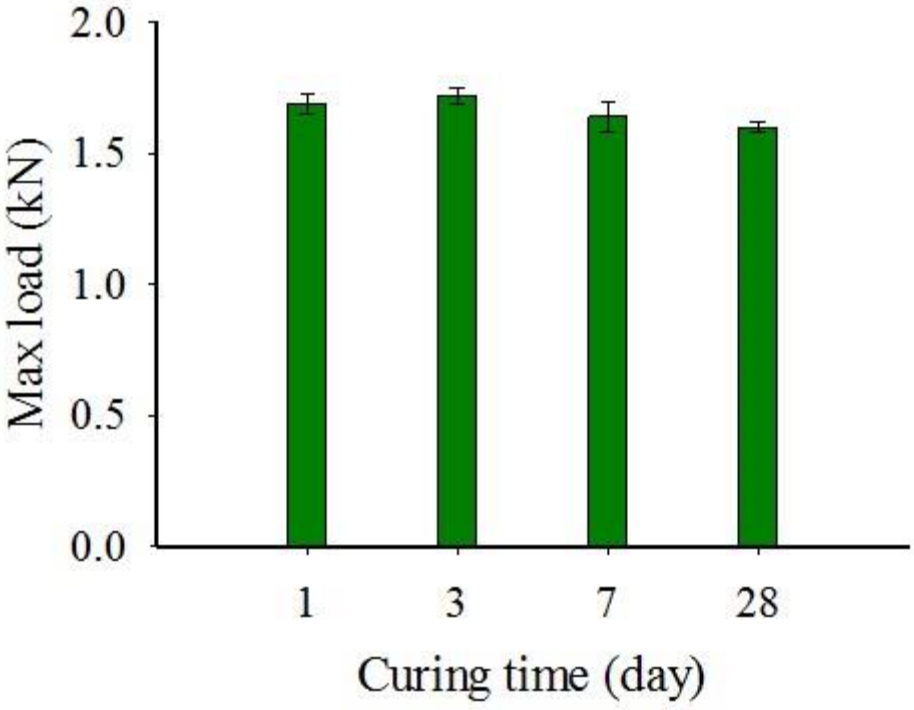

(b) Change of max puncture load by curing time

Fig. 3-11 Puncture test

3.3.8 Friction resistance test of GCCM

A 100mm × 100mm direct shear box is used to determine the shear resistance of GCCM and sand in this study. By considering the fact that the bottom layer of GCCM (i.e., woven geotextile layer) will contact directly the soil in practice, the shear tests are performed between the woven-geotextile side of GCCM and the compacted sand. The sand specimen used in this study is a dry poorly graded sand (SP) with the particle size D_{10}, D_{30}, D_{60} of 0.16, 0.19, 0.25 mm, respectively. The specimen is prepared at the dried condition with the unit weight of 14.5 kN/m^3 and the void ratio of 0.79. The tests are carried out at a constant shear rate of 0.5 mm/min in correspondence with the standard test for sand (ASTM D3080). The normal stresses are applied on specimens varied from 6 – 50 kPa, which equivalent to the vertical effective stress of soil less than 2 m depth. The direct shear test is also performed on the sand. The results from direct shear tests are presented in Fig. 3-12. The results exhibit that the angle of frictional resistance of sand (ϕ) is 38^o which is slightly higher than the frictional resistance between the GCCM and sand (δ) of 36^o. The adhesion factor can be defined as $\tan\delta/\tan\phi = 0.930$.

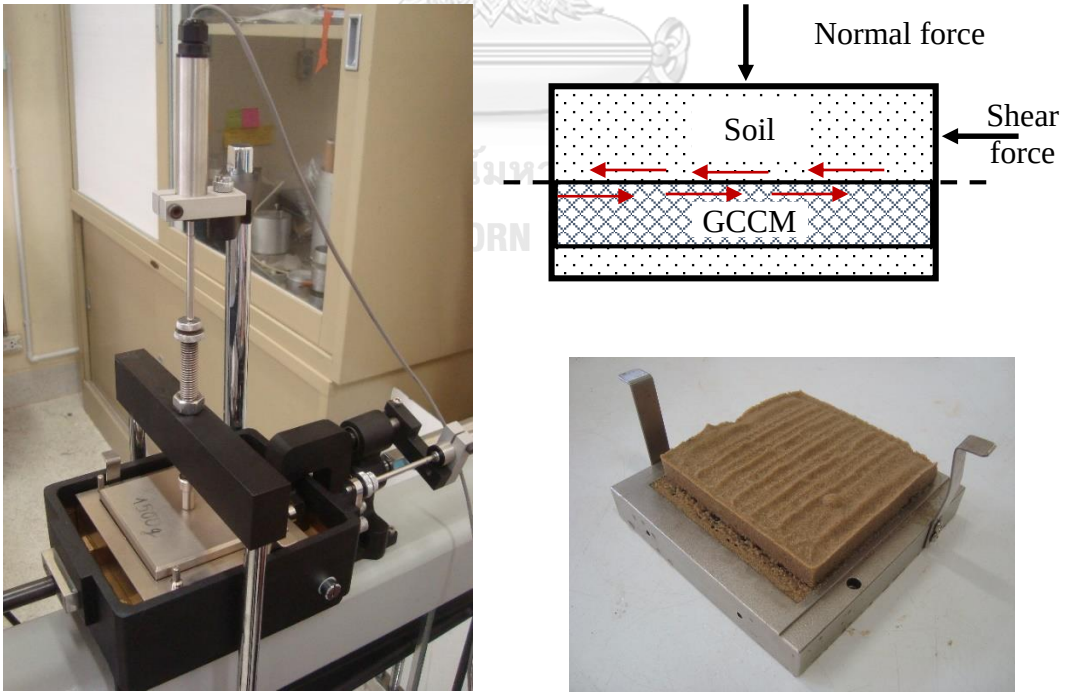

(a) Direct shear test setup for determining the friction resistance of GCCM

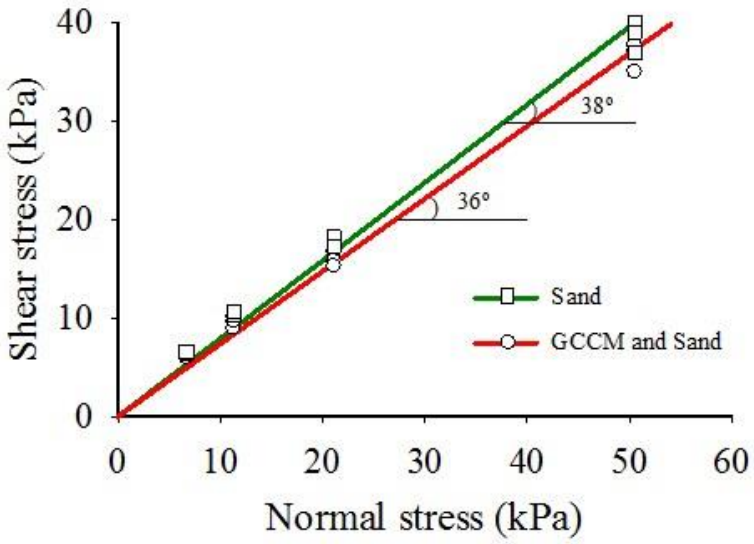

(b) Shear stress vs. normal stress

Fig. 3-12 Results of the direct shear test

It should be noted that all results presented in this chapter have published in the Journal of Construction and Building Materials (Jongvivatsakul et al., 2018)

Chapter 4: Model testing methodology

There are two types of model conducted in this study. The first model is a physical model (1-g), and the second one is a centrifuge model (25-g). For the physical model, the slope is subjected to seepage only, whereas, for the centrifuge model, the slope is subjected to both seepage and rainfall. In order to reinforce the slope, GCCM is placed directly on the surface of the slope.

4.1 Physical model tests (1-g)

4.1.1 Materials

Sand

The soil specimen used in the physical model test is a yellow fine sand taken from a river bank around 80 km north of Bangkok, Thailand. The particles smaller than 0.15 mm are removed. According to the Unified Soil Classification System (USCS), the sand is classified as poorly graded sand (SP). The distribution of particle sizes is determined by sieving method according to ASTM D422; the grain size distribution curve is shown in Fig. 4-1. The specific gravity is 2.65 and the dry unit weight and saturated unit weight in the tests are 14.5 kN/m^3 and 18.8 kN/m^3, respectively. The sand is cohesionless and the internal friction angle based on a direct shear test according to ASTM-D3080 is 38° as presented in Fig. 4-2. The average hydraulic conductivity of saturated sand with dry unit weight varying from 14.2 kN/m^3 to 14.7 kN/m^3 at 29°C, e.g., the ambient temperature in the laboratory, determined by the constant water head method, based on the standard ASTM-D2434 is 2.1 ×10^{-4} m/s, as shown in Fig. 4-3. The results show that the hydraulic conductivity is inversely proportional to dry unit weight. The properties of the sand are summarized in Table 4-1.

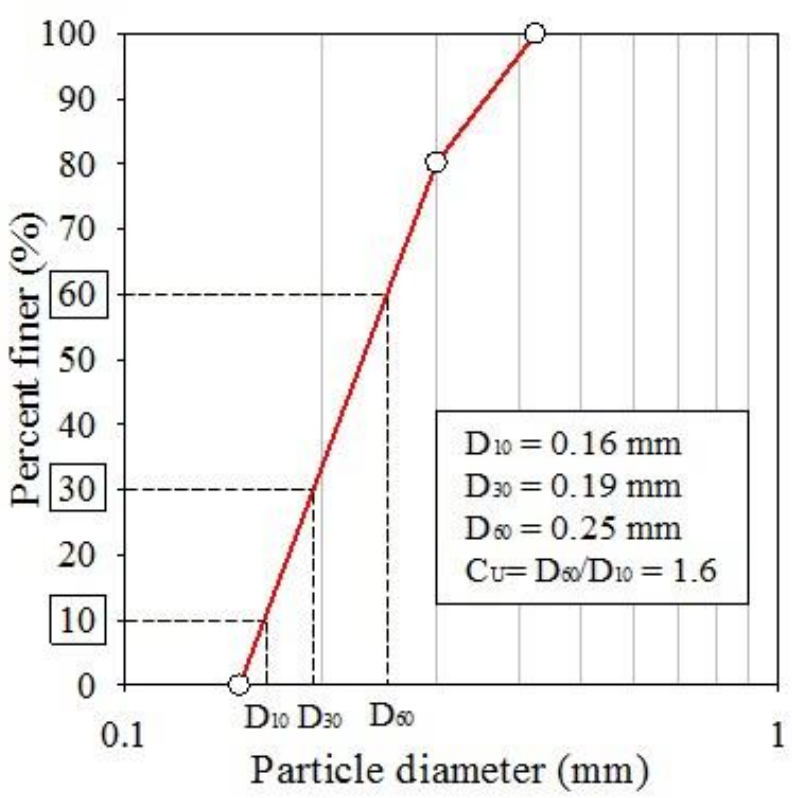

Fig. 4-1 Grain size distribution curve of sand

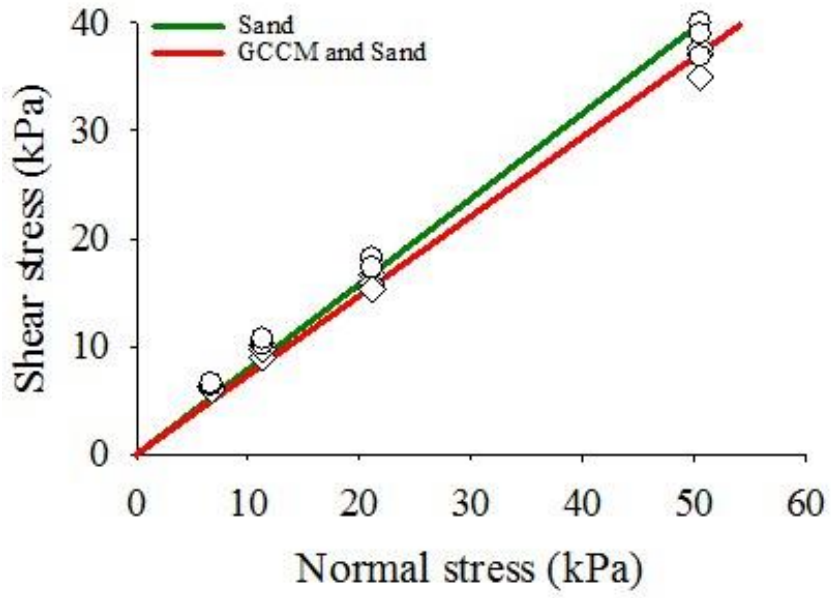

Fig. 4-2 Direct shear test results

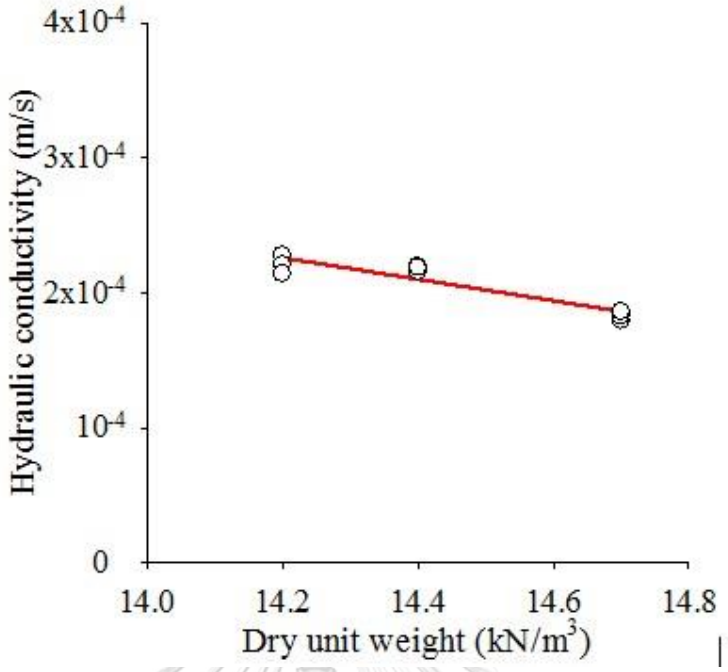

Fig. 4-3 Results of the hydraulic conductivity test

Table 4-1 Physical and mechanical properties of sand

Description	Reconstituted Sand	Unit	Standard
Grain size distribution: Sand:Silt:Clay	100:0:0	%	ASTM D422
D_{10}, D_{30}, D_{60}	0.16 - 0.19 - 0.25	mm	-
Coefficient of uniformity, C_u	1.6	-	-
Coefficient of curvature, C_c	0.9	-	-
Classification	SP	-	ASTM D2487
Dry unit weight, γ_d	14.5	kN/m^3	ASTM D7263
Saturated unit weight, γ_{sat}	18.8	kN/m^3	-
Specific gravity, G_s	2.65	-	ASTM D854
Cohesion, c’	0	kPa	ASTM D3080
Angle of internal friction, ϕ	38	°	ASTM D3080
Hydraulic conductivity, k_{sat}	2.1×10^{-4}	m/s	ASTM D2434

GCCM

The properties of GCCM used in the physical model is presented in section 3.3 of chapter 3.

4.1.2 Calibration of particle image velocimetry

OpenPIV, an open software for particle image velocimetry (PIV) analysis written in MATLAB, developed by Taylor et al. (2010), is employed to measure the displacement of soil slope. The size of interrogation area selected is 128 pixels × 128 pixels equivalent to 45 mm × 45 mm in the prototype. It should be noted that the OpenPIV gives output data in the value of horizontal and vertical velocities. Therefore, the displacement of soil is calculated by accumulation based on two such components of velocity after they are multiplied by time.

In order to evaluate the accuracy and precision of PIV technique, a series of calibration tests are carried out by using an acrylic calibration tool shown in Fig. 4-4. The calibration tool consists of two parts such as the upper box and the lower box. The upper box can freely slide on the fixed lower box. Screw bolt and dial gauge are used to control and measure the movement of the upper box in the horizontal direction, as shown in Fig. 4-4. There is also a sliding guide located on the surface of the lower box to ensure the upper box can be horizontally moved. A steel ruler is attached to the lower box surface. The calibration process is carried out on the same type of sand but different degrees of saturation (water content), in which the degrees of saturation is varied from 0% to 90%. The digital camera Canon EOS REBEL T4i/EOS 650 is used in this study. The calibration process is conducted carefully in a 3.0 m long, 2.0 m wide, and 2.0 m high chamber under the light condition induced by two LED spotlights.

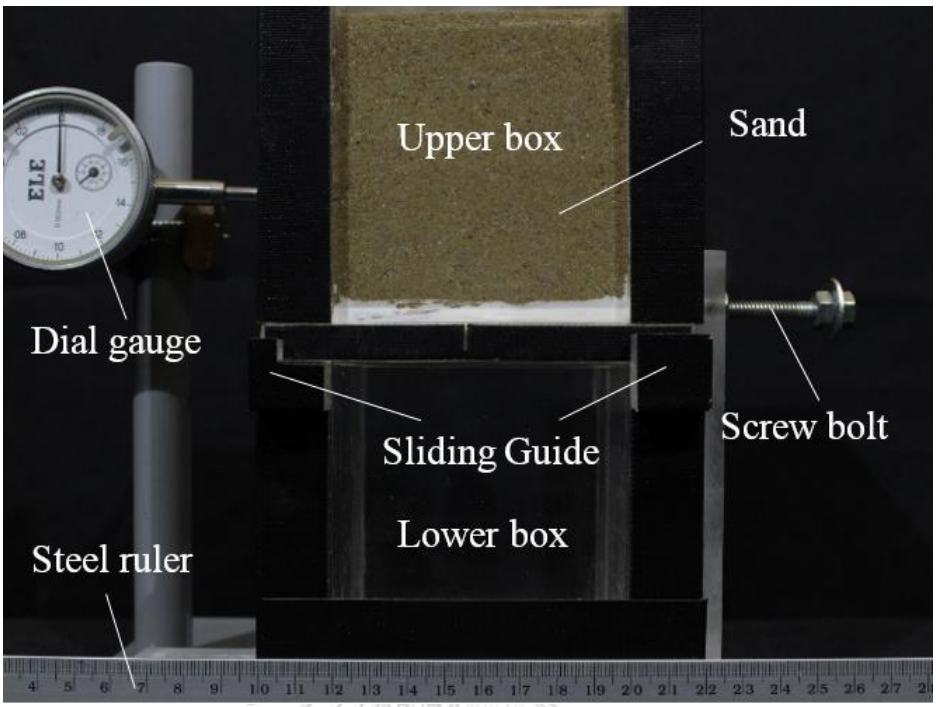

Fig. 4-4 Calibration tool

The upper box of sand is translated using the screw bolt attached to the left side of the lower box. A series of photos are captured at certain movement increments at each 1 mm. Accuracy is defined as the systematic difference between a measured value from PIV and a true value reading from dial gauge. Precision is defined as the random difference between multiple measurements of the same quantity, i.e., standard error. The calibration results show that for 128 pixels ×128 pixels patch, PIV measurement gives an average accuracy of 0.13 mm (equivalently to 2.6 pixels) and the precision of 0.005 mm (equivalently to 0.01 pixels) as presented in Fig. 4-5. It should be noted that the distortion effect is neglected in the analysis.

The accuracy can be expressed as a fraction of the field of view (FOV) width by dividing the value of accuracy, in pixels, by the image width. In that term, the accuracy can be represented as a value of $1/11.500^{th}$ of the FOV. The presently achieved accuracy is better than those of $1/5.600^{th}$ (Taylor et al., 1998) and $1/1.266^{th}$ (Paikowsky and Xi, 2000).

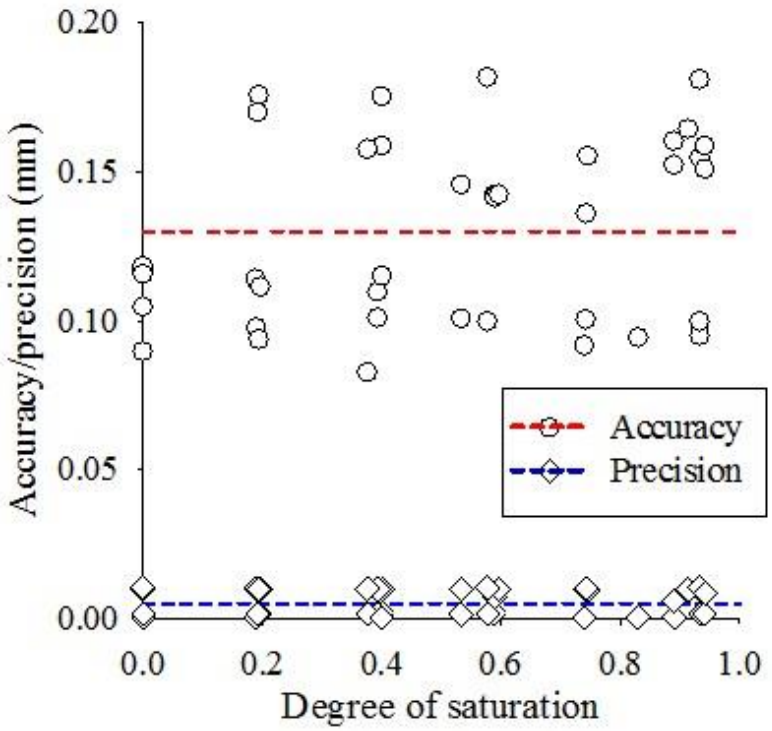

Fig. 4-5 Variation of accuracy and precision with saturation degree: red/blue dash lines stand for average accuracy and precision, respectively

4.1.3 Slope model

A 2.0 m long, 1.2 m high, and 0.2 m wide acrylic tank as illustrated in Fig. 4-6 is constructed and used for physical model tests of soil slope. All sides of the tank with a thickness of 10 mm are transparent for the purposes of monitoring and taking photos during the test. The middle section with 1.5 m in length is used to construct the slope model, while the left and right sections with 0.2 m in length are used as water supply and drainage chambers. The water chambers and the soil model are separated by perforated stainless steel walls covered with stainless wire steel mesh with opening holes of 0.1 mm to allow water move through them without washing out the soil particles. The water chambers are connected with the water supply tanks to keep the water head constant. To ensure the water supply stable and continuous, an electric pump with a capacity of 5 lit/min is used to supply water during the test. In order to measure water pressure head in the slope, two 6 mm diameter standpipes are installed along the base of soil slope. The location of two standpipes is also shown in Fig. 4-6.

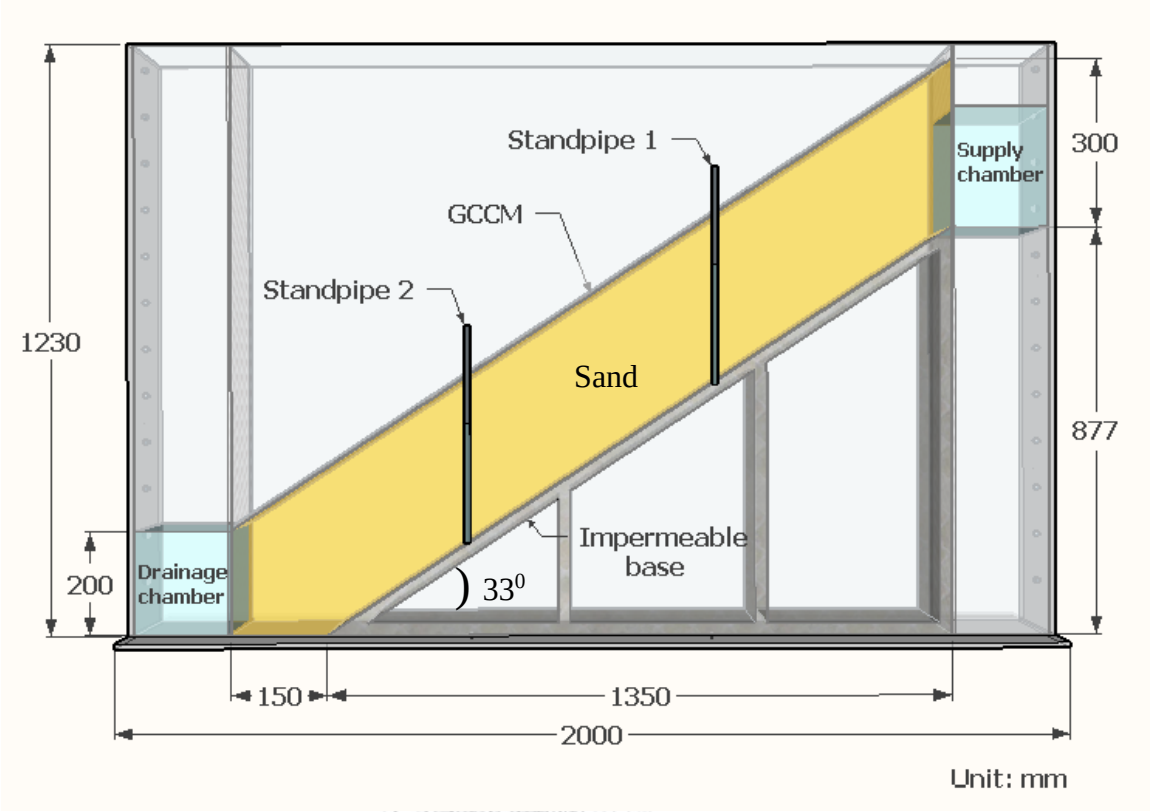

Fig. 4-6 Schematic of physical model

A sandy slope model, 1.5 m long, 0.3 m deep, and 0.2 m wide, is built onto a 33°-inclined impermeable base and a 0.15 m flat base near the slope toe. Petroleum jelly is used to put on inner surfaces of the front and back sides of the tank to reduce the friction between soil slope and both sides of the tank. Therefore, the slope model can be simplified as plane strain condition. Sand particles with size from 1 mm to 2 mm mixed with silicon glue are glued onto the top surface of the impermeable base to make a rough base.

Homogenous model sandy slopes are constructed to reach a dry unit weight of 14.5 kN/m^3. Before construction, the sand is firstly dried in the air. The dry sand is then used to construct the model slope ground. In order to make the slope ground uniformity and the test results less influenced by specimen preparation, more consistent, and repeatable, the slope is divided into 4 layers for compaction. Each layer is compacted gently with a tamping rod to obtain the target height.

A camera is set up at a distance of 2 m in front of the tank for taking photos of slope during the test. The period of the snapshot is 30 seconds. Two steel rulers are

attached to the front surface tank. It is noted that the accuracy of PIV technique used to measure the displacement of soil in this study is 0.13 mm as mentioned in the previous section.

4.1.4 Experimental program

Two experiments are carried out under the condition of seepage flow, e.g., Case 1: unreinforced slope and Case 2: reinforced slope with GCCM. In the case of slope reinforced, a GCCM sheet with 1.7 m length and 0.19 m width is put directly on slope surface. To avoid the friction between the GCCM and the acrylic, gaps of 5 mm are provided both sides. The function of these gaps is to prevent the interaction between the GCCM sheet and both sides of the tank that would affect the test result. Moreover, a 50 mm gap between GCCM and the steel mesh located at the toe is also designed to prevent them touching directly.

4.1.5 Testing procedure

The test procedure included two stages, which are half-saturation and seepage flow. Before conducting the test, the sand slope is half-saturated by applying a constant water pressure head at the upslope (h_A). After a period of around one hour, the seepage flow appears at the toe slope (h_D). It also takes about one hour to make the water pressure head at the toe slope rise up the target value of 0.2 m. Then, wait for 30 minutes, this stage aims to make the seepage flow stable. To ensure the seepage flow stable, the outlet flow rate is measured during the waiting time, e.g., for 30 minutes. Fig. 4-7 shows that the flow rate ranges from 160 to 170 ml/min at the elapsed time of 20 min. This indicates that the difference of flow rate outlet in the two cases is not significant. It is worth to note that the toe slope water pressure head (h_D) is kept a constant value of 0.2 m during the test.

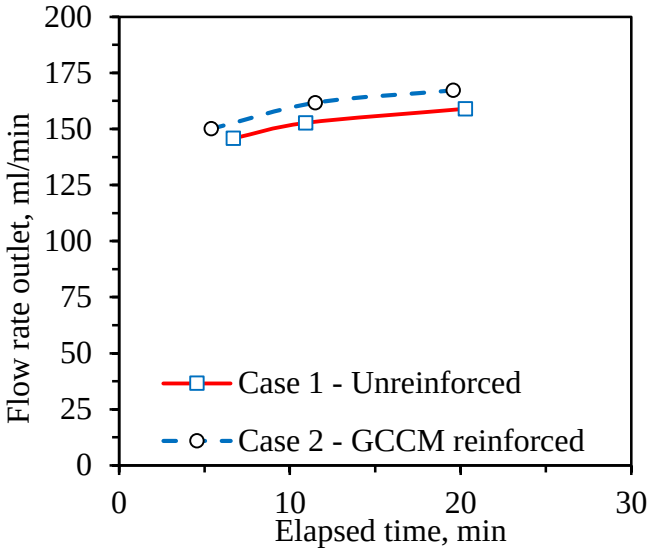

Fig. 4-7 Flow rate outlet vs. time

After the half-saturation stage, water is supplied into the supply chamber by an electric pump to raise the water head h_A gradually from the value of 130 mm. The blue dash/solid lines in Fig. 4-8 show that the average rate of rising water in Case 1 (without reinforced) is slightly smaller than that in Case 2 (reinforced). During the test, absolutely avoid disturbing the physical model and light condition because this would affect the quality of photos taken for PIV analysis. Tests are terminated when the slope is failed or the upslope water pressure head (h_A) reaches the maximum level to avoid the overflow (e.g., 250 mm).

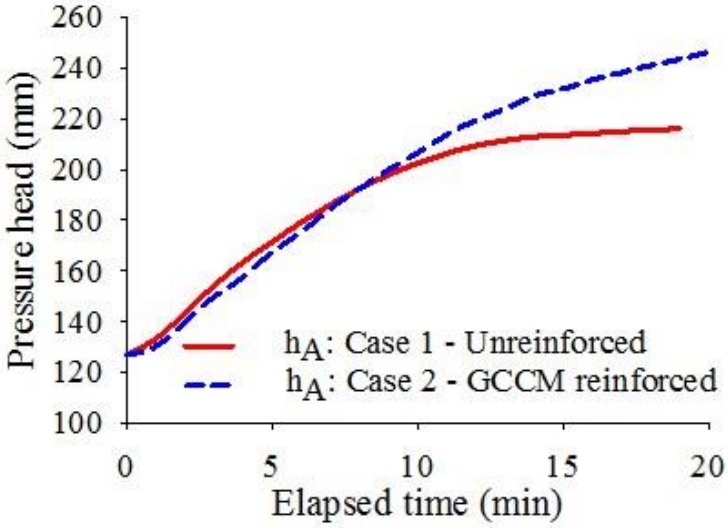

Fig. 4-8 Water pressure heads in supply chamber with time

4.2 Centrifuge model tests (25-g)

4.2.1 Equipment

4.2.1.1 Centrifuge facility

The TIT Mark III geotechnical centrifuge machine at Tokyo Institute of Technology in Japan is used in this study as shown in Fig. 4-9. The capacity and effective radius of the centrifuge machine are 100-g and 2.10 m, respectively. Dimensions of the platform are 0.90 × 0.90 × 0.97 m^3 in width × depth × height. There are 72 channels for instrumentation and 18 channels for operation. The details of this centrifuge machine can be found in Takemura et al. (1999) and Eab et al. (2014).

Fig. 4-9 Mark III geotechnical centrifuge machine

The basic scaling law for centrifuge modeling is that the stress is similar at a point in the model and that in the corresponding prototype. Table 4-2 summarizes scaling factors for various parameters in the model at N-g and prototype.

Table 4-2 Scaling factors for modeling in centrifuge at N-g

Parameter	Unit	Prototype	Model
Stress, σ	kN/m^2	1	1
Acceleration	m/s^2	1	N
Length, L	m	1	1/N
Bulk density	Ton/m^3	1	1

Cohesion, c	kN/m^2	1	1
Friction angle, ϕ	°	1	1
Interface friction angle	°	1	1
Young's modulus, E	kN/m^2	1	1
Hydraulic conductivity, k	m/s	1	1
Modulus of elasticity	kN/m^2	1	1
Rainfall intensity	mm/h	1	N

4.2.1.2 Rainfall simulator

A rainfall simulator with the dimension of 450 mm in length, 60 mm in height, and 30 mm in depth comprised of 8 pneumatic spray nozzles (BIMV45075 by H. Ikeuchi & Co., LTD) is employed to generate the artificial rain in the centrifuge model (Eab et al., 2015; Eab et al., 2014) as shown in Fig. 4-10. The nozzles can provide a spray angle of 45° and a droplet diameter of 100 μm or less (corresponding diameter of 2.5 mm or less in prototype scale). The spacing between nozzles is 50 mm. Pressure supplies including water pressure (P_w) and air pressure (P_a) are applied to provide rainfall intensity needed.

Fig. 4-10 Rainfall simulator

To calibrate the rainfall simulator, 5 rows × 10 columns array of 50 cups with 30 mm in inner diameter, and 50 mm in height are placed inside the container onto a 25°-inclined base to store rainwater from the rainfall simulator, Fig. 4-11(a). The top

of the cups is right at the surface of the model slope that will be constructed later. It is noted that these cups are placed in vertical direction and adjacent to each other. Water pressure (P_w) of 150 kPa, and air pressure (P_a) of 300 kPa are applied during the calibration process under the acceleration of 25-g. The result shows that the average rainfall intensity (I_{ave}) is 0.17 mm/s (i.e., 25 mm/h in prototype) and the coefficient of uniformity (Uc) for special distribution is 62.3%, respectively, Fig. 4-11(b). It is noted that the rainfall depth (R) = rainfall intensity (I) × elapsed time (t).

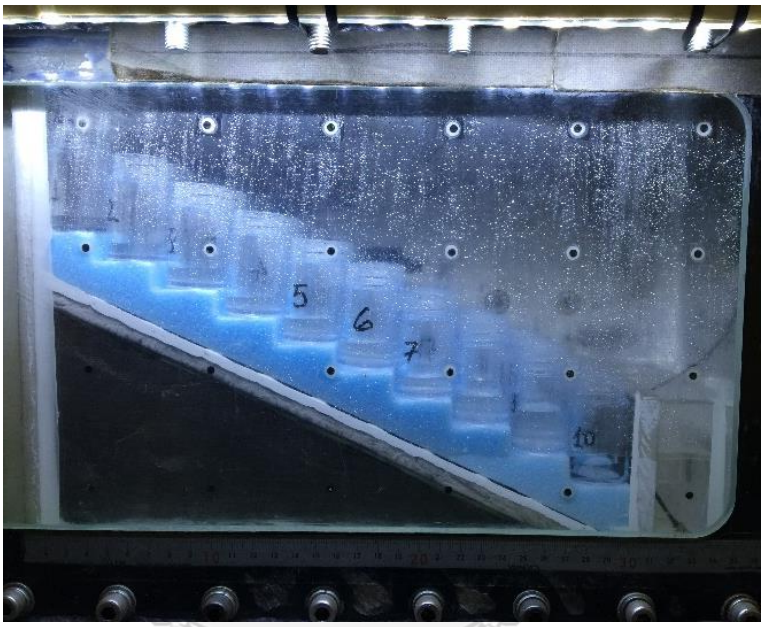

(a) Location of cups for calibrating rainfall

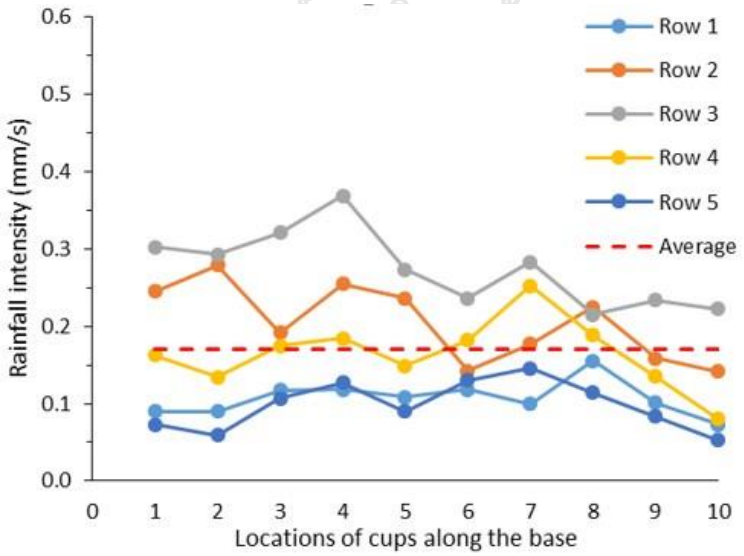

(b) Distribution of rainfall intensity in the centrifuge container

Fig. 4-11 Calibration of rainfall simulator

4.2.1.3 Measuring sensors

Pore water pressure (PWP) sensors (P303AV-2 by SSK Co., Ltd.) with dimensions of 6 mm in diameter, 8.5 mm in length are installed within the model slope to measure the pore water pressure, Fig. 4-12(a). Capacity and resolution of these sensors are 200 kPa and 0.1 kPa, respectively. Each sensor is calibrated carefully under centrifuge condition before using them.

In order to predict the horizontal displacement of soil slope, accelerometers (ACCs) (A5-50 by SSK Co., Ltd.) are used. Dimensions, capacity, and resolution of the ACCs are $5 \times 5 \times 10$ mm^3 in width × height × length, 50-g, and 0.1-g, respectively, Fig. 4-12(b). Prior to the test, each ACC is calibrated carefully.

(a) PWP sensor

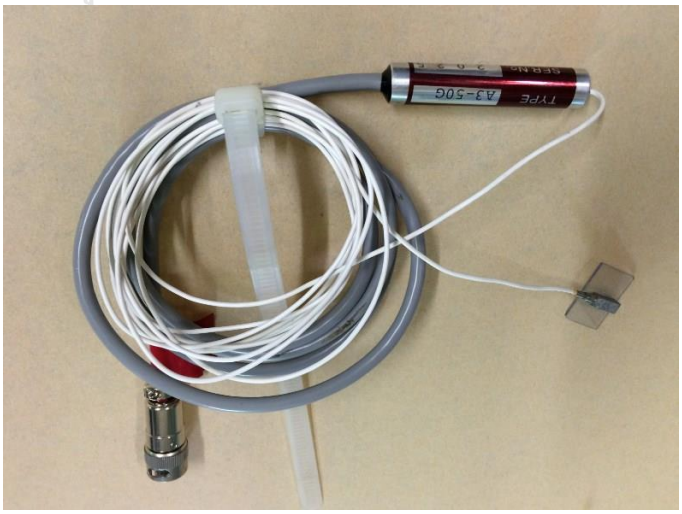

(b) Accelerometer

Fig. 4-12 PWP sensor and accelerometer

Since the accelerometers record only values of acceleration, thus, in order to predict the horizontal movement of ACCs, it is assumed that the movement manner of ACCs would be the same manner described by Orense et al. (2004), i.e., the movement is translational slide and the horizontal movement decreases by depth. By this assumption, the horizontal movement of ACCs can be predicted by integrating the inclination of accelerometers along the depth (Eab et al., 2015; Orense et al., 2004). It should be noted that each ACC is attached to a 15 mm wide by 20 mm high plastic panel. Therefore, the accelerometers move together with the soil. The horizontal displacement of soil is assumed to be caused by shear deformation of the soil, i.e., tilting of ACCs.

4.2.2 Materials

4.2.2.1 Medical gypsum plaster

It should be reminded that the highlighted characteristic of GCCM is that after hydration GCCM becomes a rigid mat with high stiffness and sealing, and the tensile strength and modulus of 28-day-cured GCCM are 3.3 MPa and 457.3 MPa, respectively. In order to simulate the behavior of GCCM in the centrifuge model, a medical gypsum plaster (MGP) sheet is selected. Scaling considerations are not only the dimension but also the stiffness and the interface friction. Basic physical and mechanical properties of the MGP such as thickness, mass per unit area, tensile strength, and interface friction are determined and summarized in Table 4-3. The tensile strength and modulus of MGP are 3.8 MPa and 470.1 MPa, respectively, which are comparable to those of the GCCM.

Table 4-3 Properties of GCCM and MGP

Properties	MGP		GCCM**
	Model	Prototype*	
Nominal thickness (mm)	0.58	14.50	8.10
Mass per unit area (g/cm^2)	0.05	1.25	1.35
Tensile strength (MPa)	3.8	3.8	3.3
Modulus (MPa)	470.1	470.1	457.3
Interface friction angle (°)	35.1	35.1	36.0

Remarks: *Prototype means applying scaling law; ** Data from Jongvivatsakul et al. (2018)

Fig. 4-13 shows a medical gypsum sheet and its result of the tensile test. It should be noted that, in order to compare the tensile strength of MGP to that of GCCM, the stress-strain curve of GCCM's tensile test is also re-plotted in Fig. 4-13 (b).

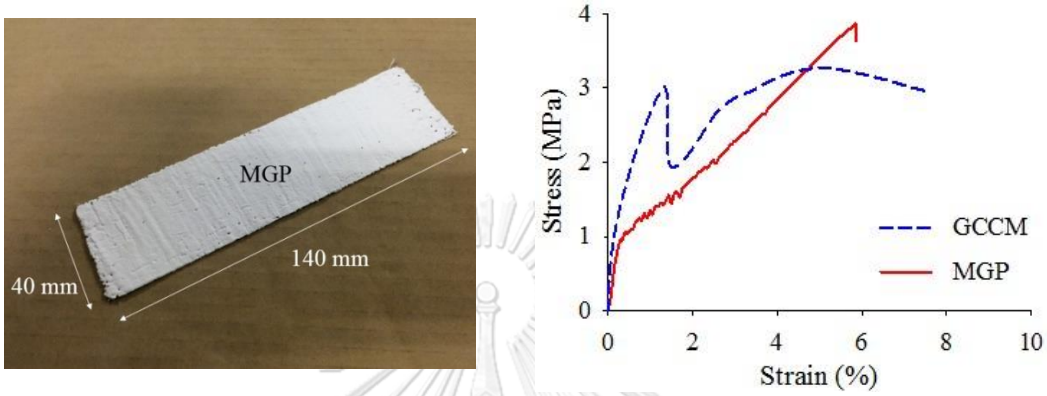

a) Medical gypsum plaster (MGP) sheet

b) Tensile stress-strain curves of MGP and GCCM

Fig. 4-13 Medical gypsum plaster (MGP) sheet and its tensile test

4.2.2.2 Silica sand

Soil used in this study is air-dried silica sand. Silica sand is mixed with water to make a water content of 15 %, and wet silica sand is cured for 24 hours before compaction. Properties of silica sand are listed in Table 4-4. Silica sand is classified as poorly graded sand (SP) based on the Unified Soil Classification System (USCS). The distribution of particle sizes is determined by sieving according to ASTM-D422-63 (1998) as shown in Fig. 4-14.

Table 4-4 Properties of silica sand

Description	Value	Unit
Grain size distribution: Sand : Silt : Clay	100:0:0	%
D_{10}, D_{30}, D_{60}	0.085, 0.12, 0.165	mm
Coefficient of uniformity, C_u	1.94	-
Coefficient of curvature, C_c	1.03	-
Classification	SP	-

Water content, W	15	%
Dry density, ρ_d	13.0	kN/m^3
Specific gravity, G_s	2.65	-
Cohesion, c’	-	kPa
Angle of internal friction, ϕ	37.8	°
Hydraulic conductivity, k_{sat}	2.4×10^{-4}	m/s

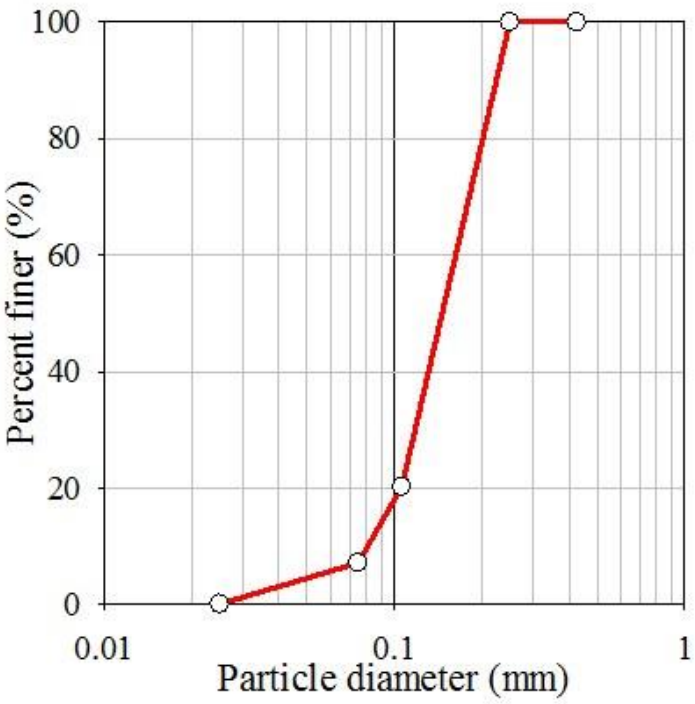

Fig. 4-14 Grain size distribution of silica sand

4.2.3 Model preparation

A 25°-inclined sandy slope with a thickness of 1.5 m and length of 7.5 m in the prototype is considered to model in the centrifuge tests. The centrifuge is spun at an acceleration of 25-g. According to the scaling law, dimensions of the centrifuge model slope are reduced to 60 mm in thickness and 300 mm in length.

A 450 mm long, 270 mm high, and 150 mm wide aluminum container is used during the centrifuge tests. The front side of the container is made of 30 mm thick transparent acrylic plate to monitor easily and take photos of slope model during the test. The container is divided into three sections. The middle section with 340 mm in

length is used to construct the model slope, the left and right sections with 80 mm and 30 mm in length are used to construct the water storage chamber (or supply chamber if seepage is applied) and the water drainage chamber, respectively. The left section and middle section are separated by an aluminum wall. In case of seepage, the separating wall is perforated and covered with geomembrane material to allow water move easily and prevent soil particles from dropping off. The water supply/drainage chamber is connected to the supply/drainage tank. The schematic view of the centrifuge slope model is presented in Fig. 4-15.

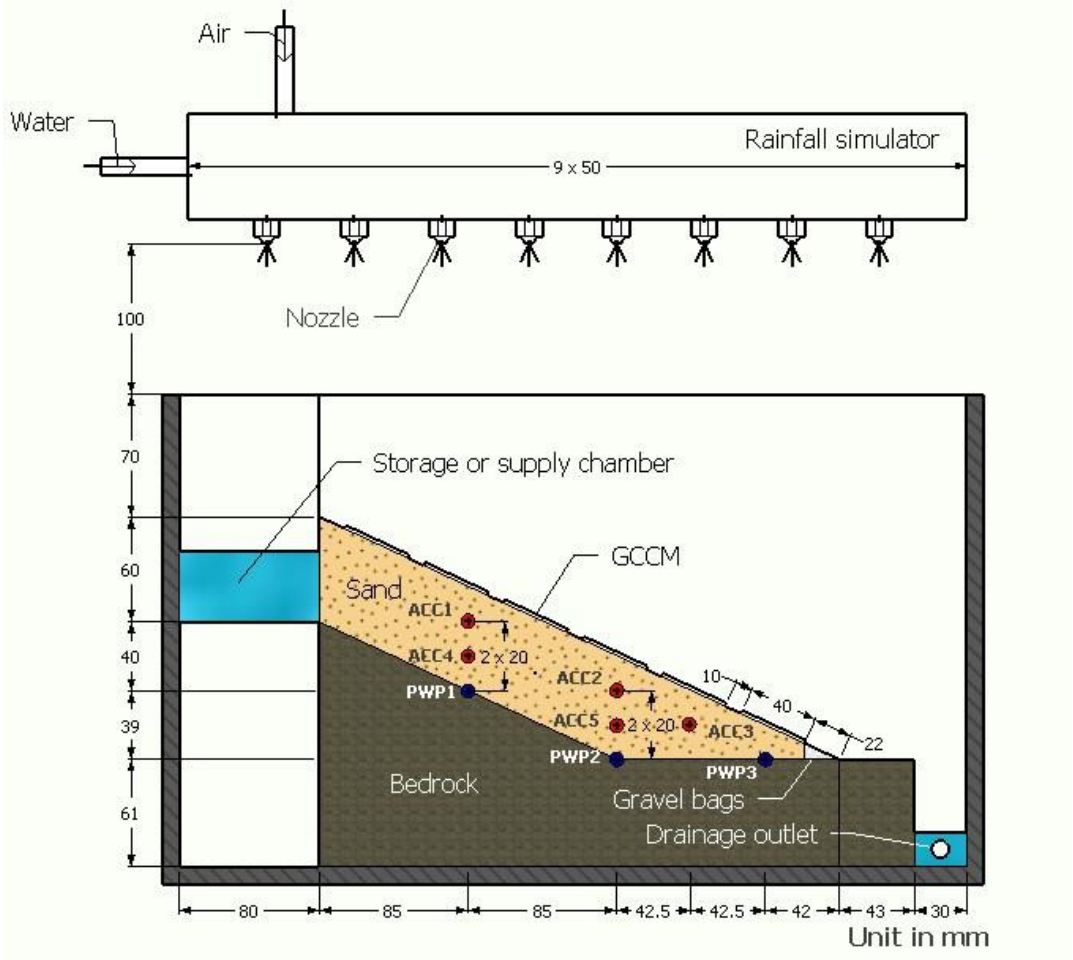

Fig. 4-15 Schematic view of the centrifuge model test

Model sandy slopes with a dimension of 300 mm long, 60 mm deep, and 150 mm wide are built onto a 25°-inclined impermeable base and a flat base near the toe as shown in Fig. 4-15. The flat base near the toe zone provides a self-stabilizing mechanism for slope stability; and by doing this, a colluvial deposit or man-made fill on hillsides is simulated (Huang and Yuin, 2010; Jiao et al., 2005; Lumb, 1975). Grease

is used to put on inner surfaces of the front and back sides of the container to reduce the friction between soil and container. The model slope can, therefore, be considered as a 2D plane strain model. In order to make a rough base, sandpaper (Fujistar CC80) is glued onto the surface of the impermeable base. In addition to sandpaper, ten 2-mm-thick acrylic strips are also fixed on the impermeable base to enhance the rough condition.

The sandy slope is prepared with a targeted-dry density of 13.0 kN/m^3 (or a degree of compaction of 90%). The under-compaction method firstly proposed by Ladd (1978) and then (Jiang et al. (2003)) is employed to control the soil uniformity and to prevent the segregation of particles. Based on the under-compaction method, the slope is divided into layers; then all layers, except the final layer, are compacted to a lower density than the target density of the slope. In this study, the slope is divided into 3 layers with 20 mm thick each. The 80% and 75% compaction are applied for the first and second layers, respectively (Jiang et al., 2003).

Since seepage could wash out sand particles at the edge of the slope toe and causes local initial failure, which may lead to being difficult in assessing the effect of GCCM on slope stability. In order to minimize the local failure at the toe slope, 10 small gravel bags with a weight of 3.2 g (i.e., 50 kg in the prototype) are placed at the slope toe. The length, height, and width of gravel bag are approximately 15 mm, 10 mm and 15 mm (i.e., 37.5 cm, 25 cm and 37.5 cm in the prototype), respectively. It should be noted that the purpose of this study is to observe the benefit of GCCM on slope failure, so the initial failure at the toe slope shall be prevented.

Three PWP sensors are placed at the base of the model and five accelerometer sensors are installed at depth of 20 mm and 40 mm as depicted in Fig. 4-15. All sensors are connected with an acquisition data system to record signals at every 0.1 sec. It should be noted that all pore water pressure sensors are saturated with silicone oil for 2 hours before being embedded within soil slope. The rainfall simulator is placed at 100 mm above and center of the container. Two cameras are also installed at the front and top of the model slope to monitor during the test.

4.2.4 Experimental program

Four centrifuge model tests, denoted as Case 1: unreinforced slope under seepage, Case 2: GCCM reinforced slope under seepage, Case 3: unreinforced slope under rainfall, and Case 4: GCCM reinforced slope under rainfall are performed as summarized in Table 4-5. The purpose of conducting the centrifuge model tests is to evaluate the different deformation and infiltration characteristics of the slope under both seepage and rainfall conditions.

In fact, the full covered GCCM placed on the slope surface may not be efficient and economic. The coverage ratio, which is defined by the ratio between the total area of GCCM and the slope surface area, of 75% is selected in this study. In case of slope reinforced with GCCM, 6 MGP sheets with a dimension of 40 mm × 140 mm are placed on the slope model surface with a spacing of 10 mm.

For the seepage case, the water supply tank is opened after initial spinning. The targeted water head of 45 mm (i.e., 1.13 m in the prototype) is selected in this study. The rainfall intensity of 0.17 mm/s (i.e., 25 mm/h in the prototype) is used for the rainfall case.

Table 4-5 Summary of centrifuge experiments

Case	Description	Condition	Water head (mm)	Rainfall intensity, I (mm/s)	Test duration, t (min)	Deformation
1	Unreinforced	Seepage	45.3	-	10.7	Collapsed
2	With GCCM	Seepage	44.0	-	23.3	Collapsed
3	Unreinforced	Rainfall	-	0.17	3.0	Moderate; Not collapsed
4	With GCCM	Rainfall	-	0.17	3.0	Very small; Not collapsed

Remarks: All values are measured in the model.

Chapter 5: Physical model testing results and numerical simulation

Based on results of water pressure head observed from two standpipes and water levels in the chambers located at the crest and toe of the model slope and based on results of displacement measured by PIV technique, interpreting the change of water pressure head and of displacement is focused in this section. In addition, numerical simulation and the discussion are presented as well.

5.1 Water pressure head

The water pressure heads at the position of A, B, C, and D located at the supply chamber, standpipe 1, standpipe 2, and drainage chamber, respectively, as shown in sub-figure of Fig. 5-1, are observed by means of the photos taken. By this mean, the change of water pressure heads with time can be recorded. Fig. 5-1 shows the change of water pressure heads at the position of A, B, C, and D for Cases 1 and 2. It can be seen that there are simultaneous increases in water pressure heads within the slope with the water supply at the upslope in both cases. Especially, the pressure head at location B increases more quickly than that at location C. This may be attributed to head loss since point C is further the supply chamber than point B. In addition, it can be seen that the pattern of change of pressure head at A, B, C, and D in both cases is quite the same. This result suggests that the properties of sand and the hydraulic condition in both cases are similar.

For Case 1, at the elapsed time of 7 min, i.e., at the time when the pressure head at location A reaches 186 mm, the movement of the crest of the slope is observed visibly. It is also interesting to note that the water pressure head at point B starts increasing rapidly a half minute later, i.e., the elapsed time is 7.5 min, while the pressure head h_A still increasing gradually. This observation suggests that the movement of the slope has affected to the increase of pressure head h_B. In contrast to Case 1, the movement of the slope crest is not observed until the elapsed time is 15 min in Case 2. The increase of pressure water head at point B is gradual till the test terminated in Case 2.

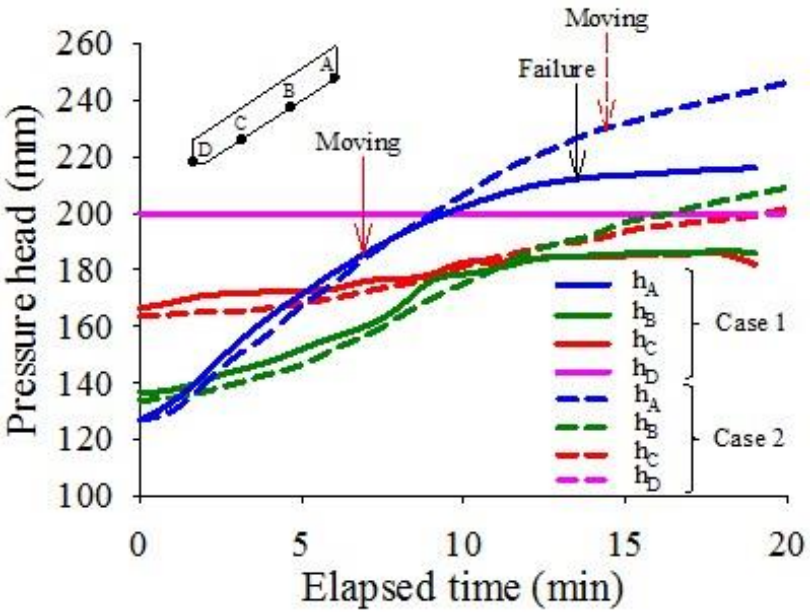

Fig. 5-1 Variations of water pressure heads with time

5.2 Displacement

In order to interpret the deformation of soil slope, 8 vertical and 13 oblique cross sections are considered, as shown in Fig. 5-2. The spacing between vertical cross sections and the spacing between oblique cross sections are 180 mm and 22 mm, respectively.

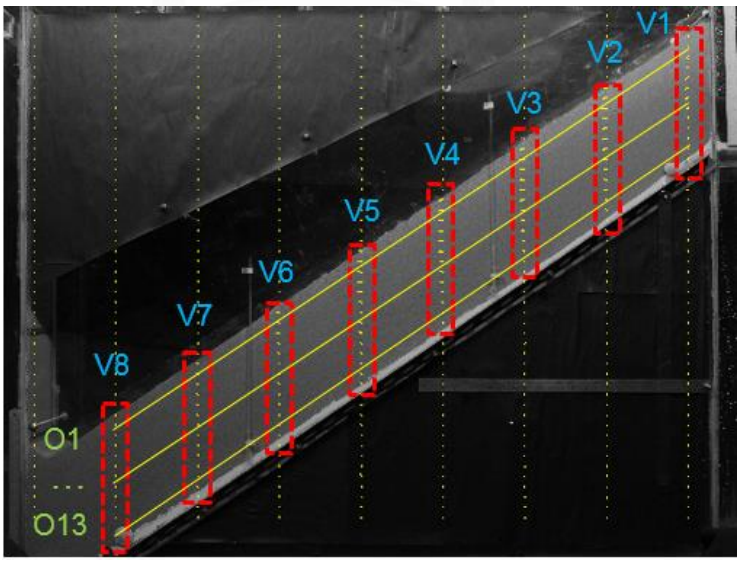

Fig. 5-2 Locations of cross sections

Fig. 5-3 shows the displacement vs. upslope water pressure head (h_A) curves of soil slope at vertical-cross section V3 at different depths of 22, 66, 110, 154, 198, 242, and 286 mm. It can be seen that the displacement of soil is increased with pressure head h_A. The maximum displacements of soil in Cases 1 and 2 are 45 and 7 mm, respectively. The significant reduction of displacement in Case 2 indicates that GCCM has contributed to the deformation of the slope.

For Case 1, slope displaces rapidly when upslope pressure head (h_A) reaches a value of 213 mm (about 71% compared to the depth of the model slope) as shown in Fig. 5-3(a). In contrast, the displacement of slope in Case 2 is still gradually changed when h_A reaches 213 mm, even when h_A reaches a high value of 246 mm as shown Fig. 5-3(b). This proves that GCCM has contributed to the resistance of slope and made the deformation decrease. The displacement of soil at the other vertical-cross sections is also similar to the section V3 but with smaller magnitude. At all vertical-cross sections, the movement of soil at depth of 286 mm is very small which comes from the roughness of the base.

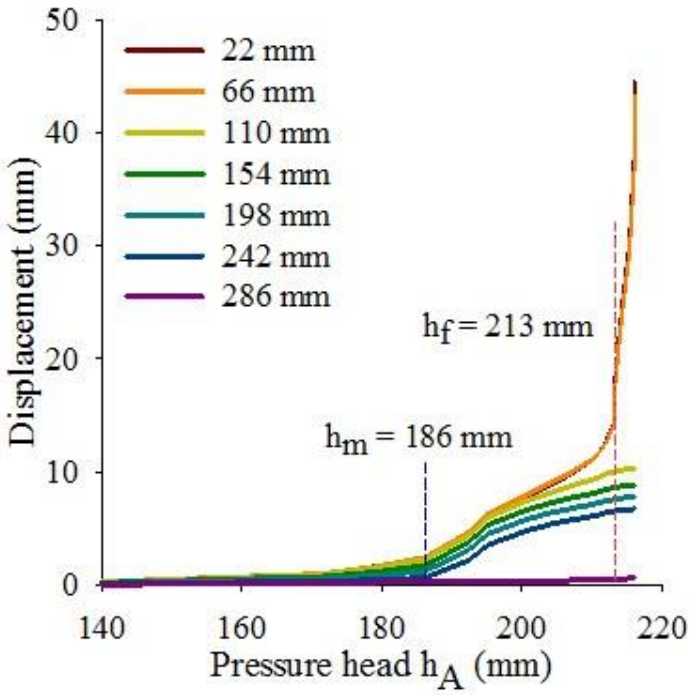

(a) Case 1: without reinforcement

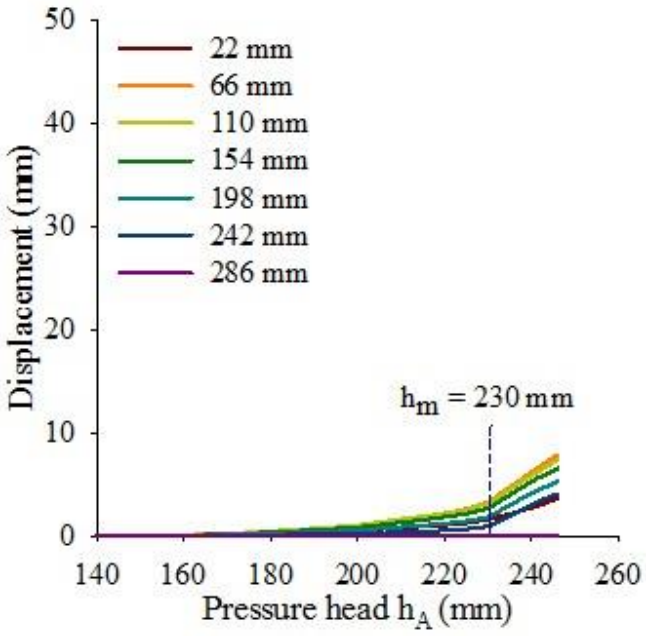

(b) Case 2: with reinforcement

Fig. 5-3 Displacement of soil at vertical-cross section V3

The typical shape of the displacement and water pressure head curve at shallower depth can be illustrated in Fig. 5-4. Based on the curve, two sudden change points (denoted as P_m and P_f) could be identified. The pressure heads at P_m and P_f (denoted as h_m and h_f) can be defined as the pressure heads when the slope starting moving and failure, respectively. According to the definition, h_m and h_f could be determined. For Case 1, h_m = 186 mm and h_f = 213 mm; for Case 2, h_m = 230 mm and h_f cannot be determined because of no failure.

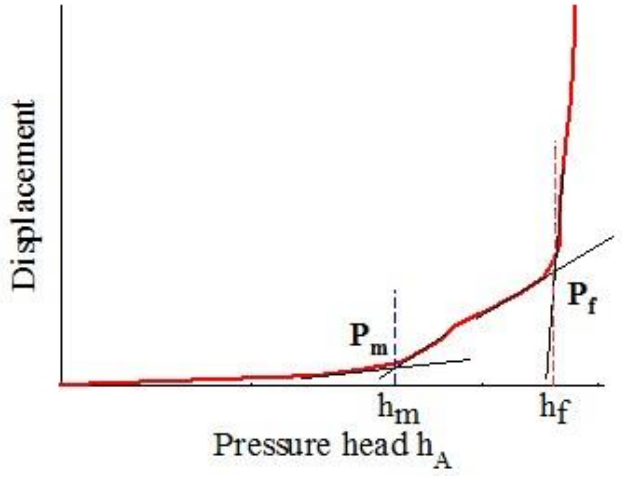

Fig. 5-4 Typical displacement and water pressure head curve

In order to interpret the variation of displacement with depth, the displacement of soil slope is re-plotted as shown in Fig. 5-5. In Case 1 without reinforcement, the movement of soil near the surface is larger compared to those of beneath part, as shown in Fig. 5-5(a). In contrast, in Case 2 with reinforcement by GCCM, the displacement of soil tends to be small at the surface and increases to a certain depth, finally decreases with depth, as shown in Fig. 5-5(b). The maximum movement near the surface in Case 1 and Case 2 when h_A equals to 216 mm are 44 mm and less than 5 mm, respectively. The difference in displacement is very large, approximately greater than 8 times.

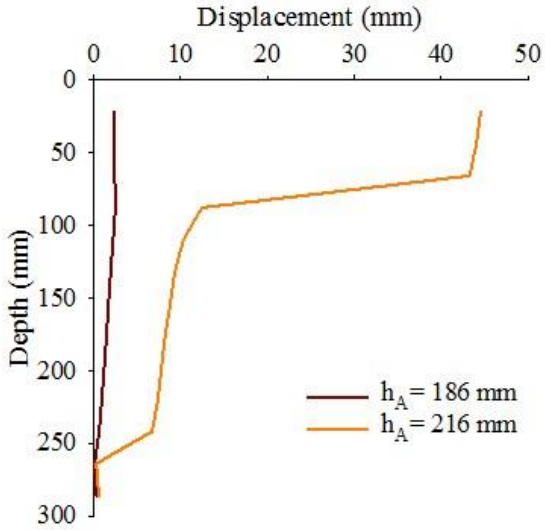

(a) Case 1: without reinforcement

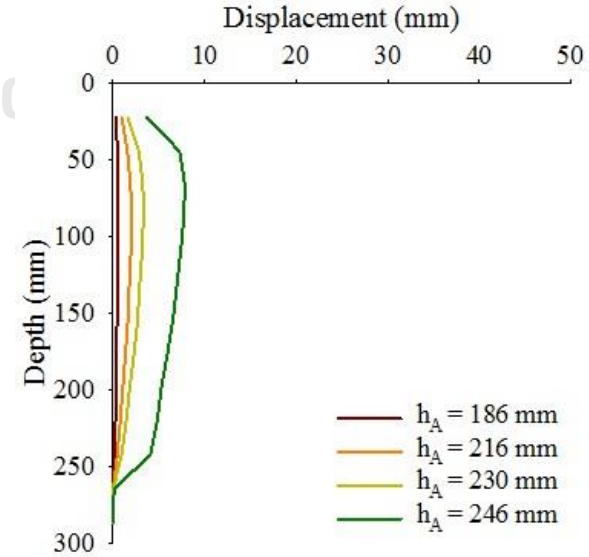

(b) Case 2: with reinforcement

Fig. 5-5 Variation of displacement by depth at section V3

The direction of movement of soil slope can be presented in terms of the velocity vectors of soil particle derived from the OpenPIV as illustrated in Fig. 5-6. The results indicate that the major direction of movement is nearly parallel to the base of the slope. In addition, the failure zone can be detected by the velocity vector as shown in Fig. 5-6(b). The depth of failure zone varies from section to section and tends to be deeper at the upslope and shallow at the downslope. The maximum depth (D) and length (L) of failure zone are about 0.1 m and 1.7 m, respectively. The D/L ratio of 6% can be classified as a translational failure according to Abramson et al. (2002) and Hansen (1984).

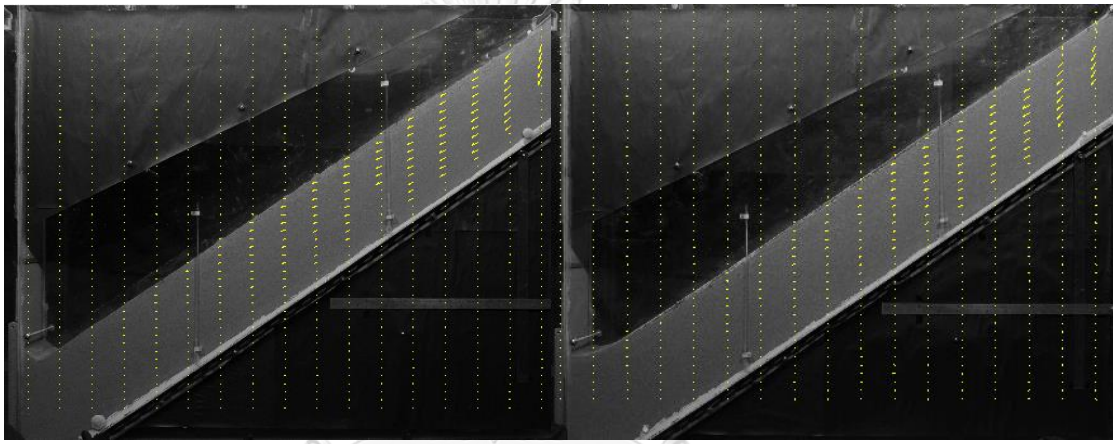

(a) Case 1 at h_A = 186 mm (c) Case 2 at h_A = 230 mm

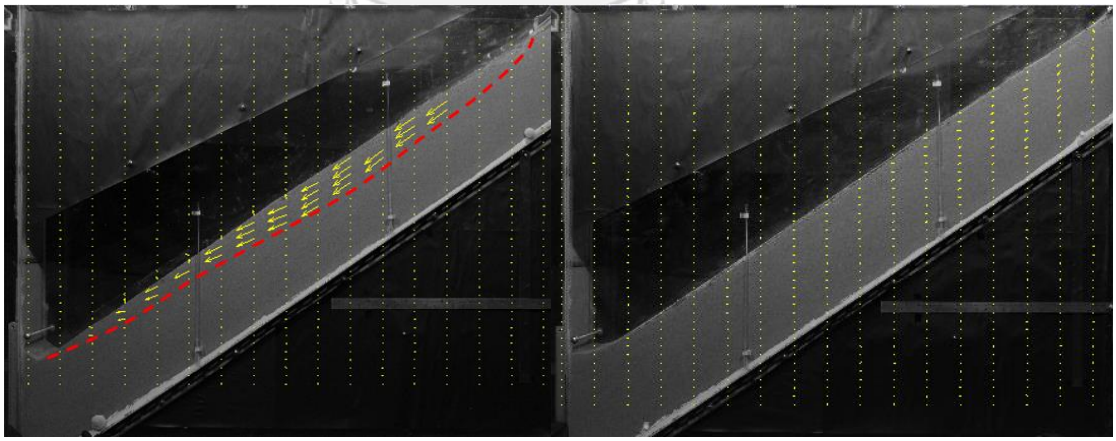

(b) Case 1 at h_A = 213 mm (d) Case 2 at h_A = 246 mm

Fig. 5-6 Velocity vectors of soil particle

When the test is terminated, the photos are taken on the soil slope as shown in Fig. 5-7. The unreinforced slope is absolutely failed after the test, but the reinforced slope with GCCM is still stable.

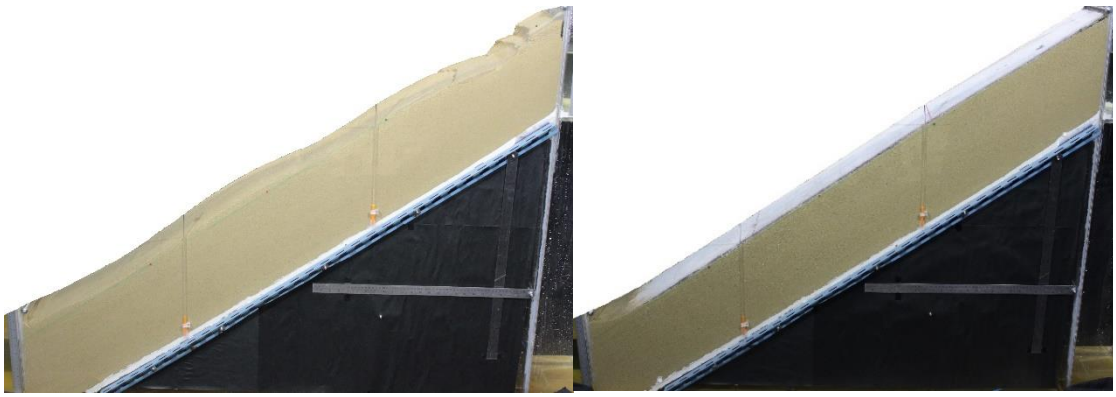

(a) Case 1: without reinforcement (b) Case 2: with reinforcement

Fig. 5-7 Photos of soil slope after the test

5.3. Numerical simulation

In order to understand more about the effects of GCCM on the slope stabilization, a series of numerical simulations are conducted using PLAXIS 2D. By using this software, GCCM can be modeled as a solid elastic structure called *Plate*. The input parameters of GCCM are presented in Table 5-1. It should be noted that young modulus, E, is obtained from the tensile test in the length direction of GCCM after curing 7 days.

Table 5-1 Input parameters of GCCM

Parameter	Symbol	Value	Unit
Material type	Type	Elastic	-
Structure type	Plate	Elastic	-
Young modulus	E	240800	kPa
Thickness	d	8	mm
Nominal stiffness	E × A	1926.400	kN/m
Flexural rigidity	E × I	0.010	kN × m^2/m
Weight	w	0.132	kN/m/m
Poisson's ratio	ν	0.25	-

The interaction between GCCM and slope surface plays an important role in slope stability. To quantitative this interaction, the interface friction angle is defined and determined using the direct shear test as shown in section 3.3.8. In Plaxis 2D, there is a factor called R_{inter} which can be used to describe the interface friction of two

materials' surfaces acting on together. R_{inter} is defined as a ratio of tanδ/tanϕ (e.g., 0.93). Where, δ is the interface friction angle, and ϕ is the friction angle of sand.

To simulate the behavior of sand layer, Mohr-Coulomb model is selected, and drainage type is drained. Table 5-2 shows input parameters of sand. Young modulus and friction angle of sand are obtained from oedometer test and direct shear test, respectively. Under the drained condition, the cohesion of sand is assumed very small nearly zero.

Table 5-2 Input parameters of sand

Parameter	Symbol	Value	Unit	Note
Material model	Model	Mohr-Coulomb	-	-
Drainage type	Type	Drained	-	-
Unit weight above water level	γ_{unsat}	16.7	kN/m^3	Unsaturated sand affected by capillary
Unit weight below water level	γ_{sat}	18.8	kN/m^3	Measured
Young modulus	E'	366	kPa	From oedometer test – normal stress from 0 to 6.7 kPa
Poisson's ratio	ν'	0.33	-	Typically Poisson's ration of sand
Cohesion	c'	0.6	kPa	Small cohesion
Friction angle	ϕ'	38	Degree	From the direct shear test
Dilatancy angle	ψ	8	Degree	Predicted using ψ = ϕ' – 30

The numerical model of the slope is divided into 1881 elements, and the boundary conditions are applied to the model. Type of boundary AB, CD, DE, and EA

are assigned as shown in Table 5-3. Location of each boundary is presented in Fig. 5-8. It is worth to note that soil along boundary CD can move horizontally toward the left side (free boundary), but it cannot move toward the right side (fixed boundary). Plaxis 2D does not allow to model that boundary condition, i.e., the boundary is not only free in the horizontal direction but also fixed in horizontal direction. Therefore, the boundary CD is assigned as fixed horizontal displacement.

Table 5-3 Boundary conditions of the numerical model

Boundary	Seepage	Horizontal displacement	Vertical displacement
AB, CD	Seepage	Fixed	Free
DE, EA	Closed	Fixed	Fixed

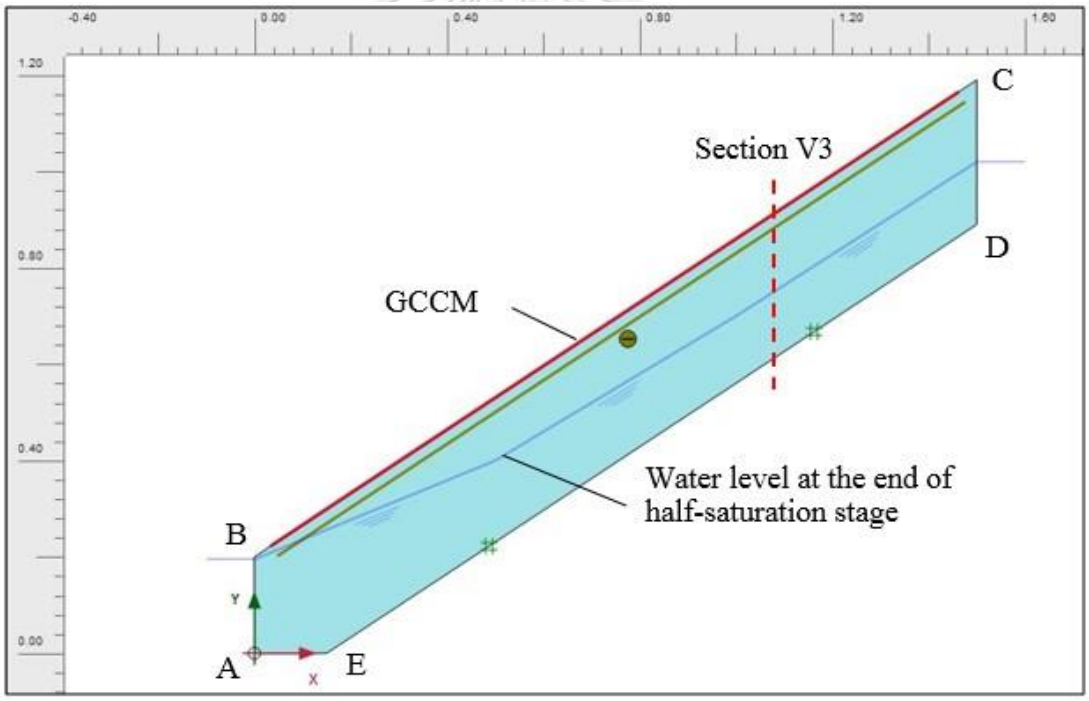

Fig. 5-8 Schematic of the numerical model constructed in Plaxis 2D

The numerical simulation is strictly followed the testing procedure of physical model test mentioned before, which is described in section 4.1.5. Firstly the water level in the numerical model is set as same as the one in the physical model, e.g., h_A = 130 mm and h_D = 200 mm, and then the water level at the upper slope (h_A) is raised up to a target value of 250 mm, as seen in Fig. 5-8. Hence, the hydraulic force acts on the slope and makes the slope displace.

The total displacement of slope obtained from numerical simulation is displayed in Fig. 5-9. This figure shows that the displacement occurs mainly at the upper slope, and it becomes smaller toward to the toe of the slope. In case of the slope without GCCM, the slope fails when pressure head h_A reaches a value of 243 mm, but slope reinforced with GCCM is still stable even though h_A reaches the target value of 250 mm. The failure zone from Fig. 5-9(a) is similar to that observed from the physical model test, e.g., Fig. 5-6(b), except the difference of the failure depth deeper.

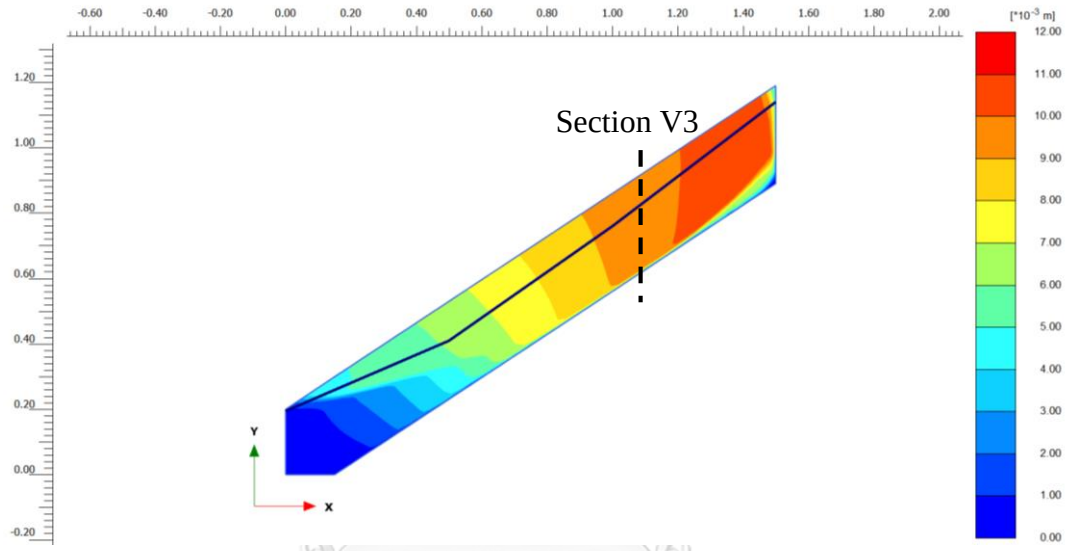

(a) Case 1: without GCCM at h_A = 243 mm

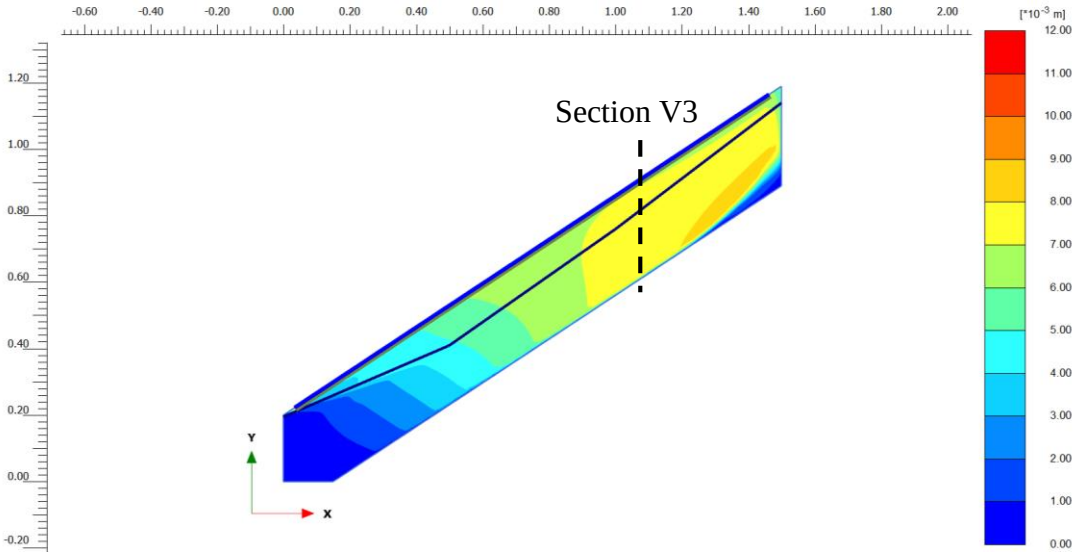

(b) Case 2: with GCCM at h_A = 250 mm

Fig. 5-9 Total displacement of the slope with/without GCCM obtained from 2D numerical simulation (Plaxis)

Additionally, the change of displacement by depth at cross-sectional V3 is presented in Fig. 5-10. It can be seen that the displacement tends to increase by depth in case of the slope with GCCM (from 6.80 mm to 7.73 mm), while the displacement tends to decrease slightly by depth in case of the slope without GCCM (from 9.55 mm to 9.47 mm). This pattern of displacement is consistent with that obtained from the physical model test.

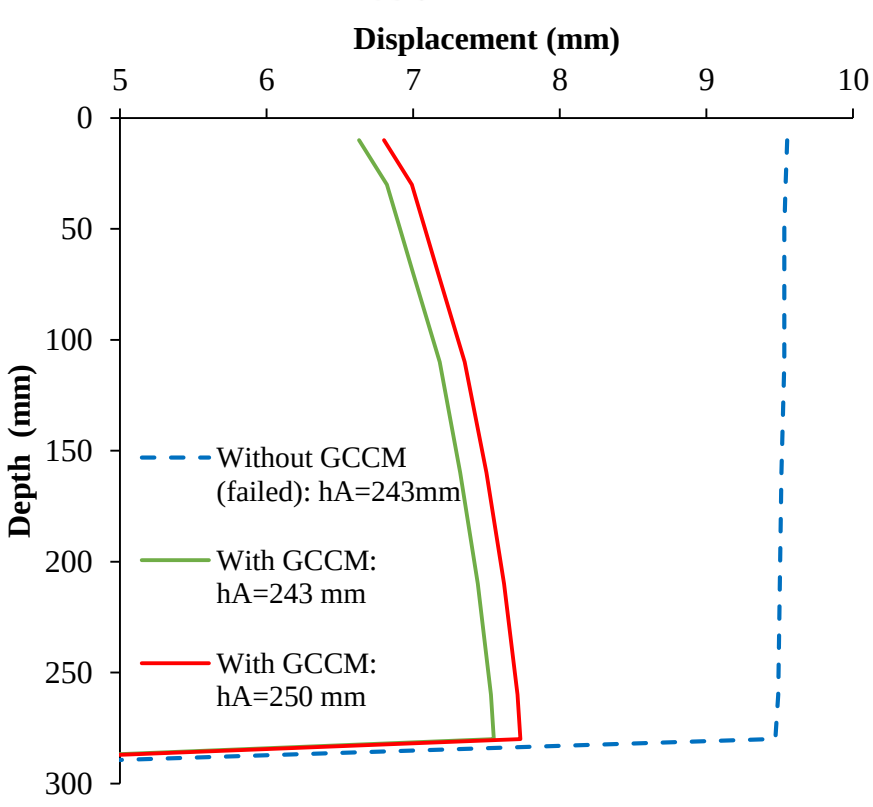

Fig. 5-10 Change of total displacement of slope reinforced with/without GCCM by depth at cross-sectional V3

Hence, these results presented above indicate that the presence of GCCM makes the deformation characteristics of slope change, and GCCM can reinforce the slope significantly, i.e., the slope reinforced with GCCM more stable.

With the purpose to compare the results between the physical test and the numerical simulation, the change of displacement vs. pressure head (h_A) curves at 66 mm depth of cross-sectional V3 are plotted together as shown in Fig. 5-11. It can be

seen that when pressure head h_A is less than 190 mm, the results obtained from the numerical simulations are close to those obtained from the physical model test. However, when h_A is greater than 190 mm, the difference of results between the numerical and physical model is very large especially in case of the slope without GCCM. It maybe comes from the limitations of the numerical simulation. That is, in fact, Plaxis 2D cannot model exactly all conditions in the physical model.

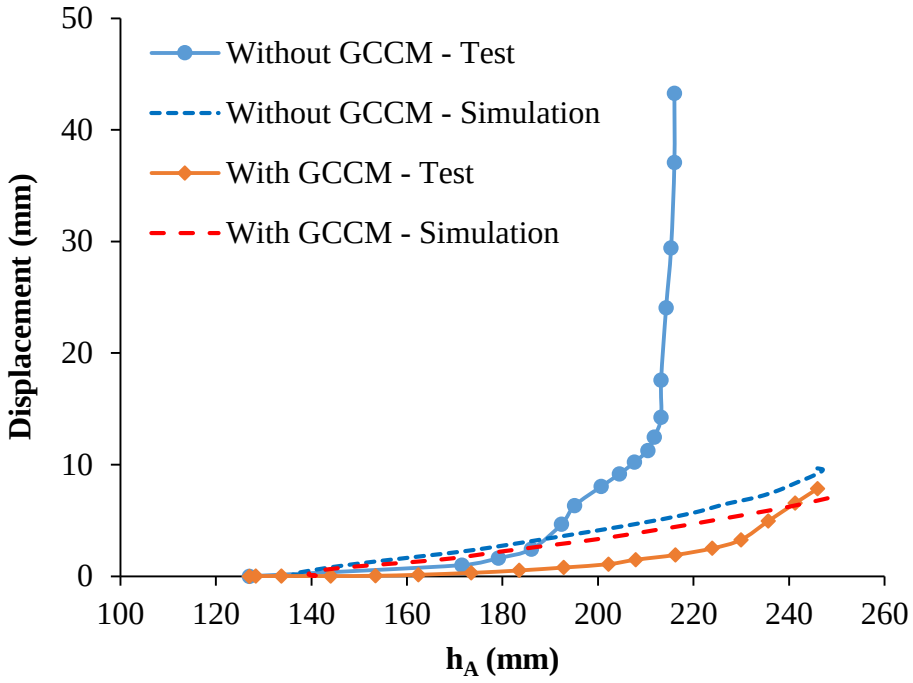

Fig. 5-11 Change of total displacement by pressure head, h_A, at 66 mm depth of cross-sectional V3

Additionally, the safety factor of the slope without/with GCCM after conducting the half-saturation stage is also predicted by Plaxis 2D. The results show that they are 1.20 and 1.24, respectively.

In order to assess the effect of GCCM's stiffness on the deformation and stability of the slope reinforced with GCCM, a series of numerical simulations are conducted by considering the varying stiffness of GCCM. The results show that the displacement and the stiffness of GCCM are reverse, i.e., if the GCCM's stiffness increases, the displacement will decrease, Fig. 5-12. In addition, the effect of GCCM on deformation of the slope is reduced with depth, Fig. 5-12(b). It should be noted that

the ratio of E_{GCCM}/E_{soil}, in Fig. 5-12, is used to normalize the stiffness of GCCM, e.g., E_{GCCM}/E_{soil} equals 1, 100, 200, 400, and 800.

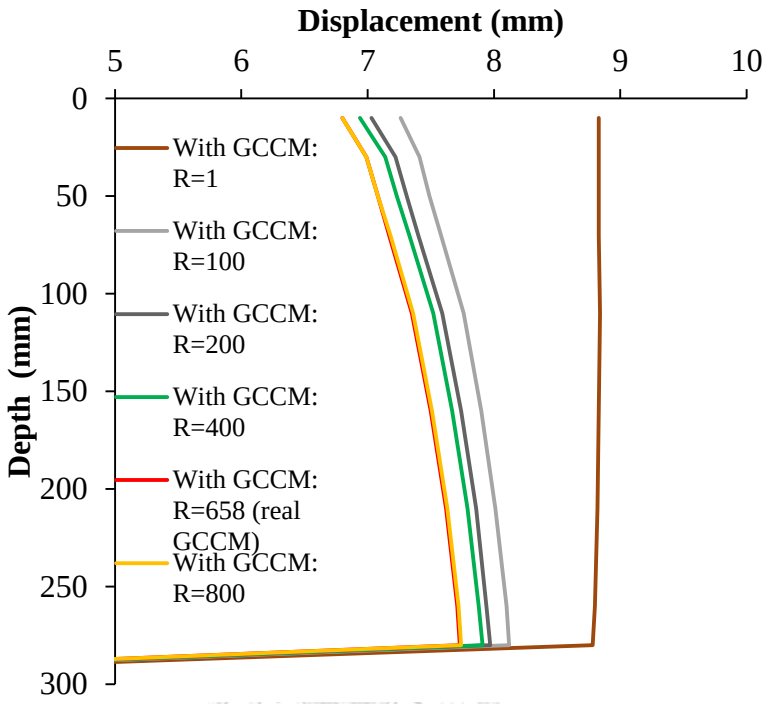

(a) Change of total displacement by depth at section V3, when h_A = 250 mm, by varying stiffness of GCCM; Noted that R = E_{GCCM}/E_{soil}

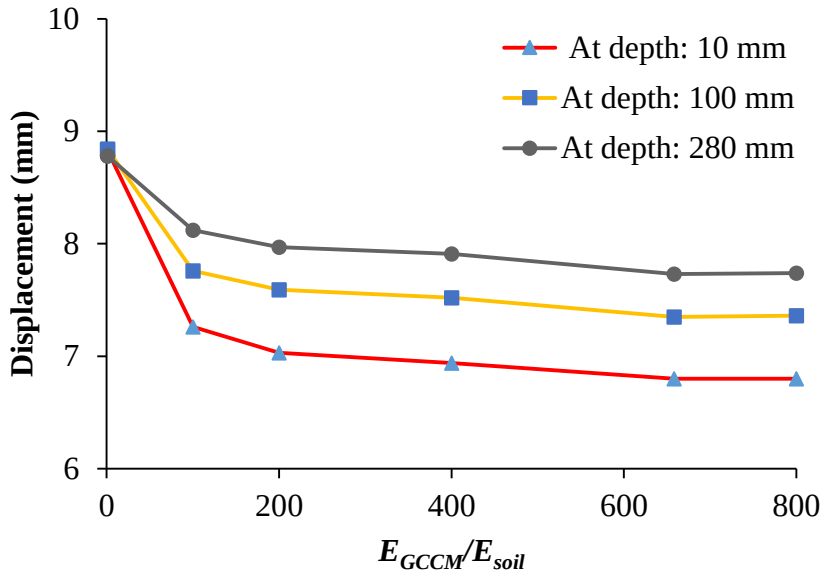

(b) Change of total displacement vs. ratio of E_{GCCM}/E_{soil}, when h_A = 250 mm

Fig. 5-12 Change of total displacement when varying the stiffness of GCCM at section V3

Furthermore, to evaluate the effects of the interface friction between GCCM and slope surface on the deformation and stability of slope reinforced with GCCM, a series of numerical simulations are conducted by considering the varying the interface friction angle through ratio of tanδ/tanϕ, e.g., 0.2, 0.3, 0.4, 0.5, 0.6, 0.7, 0.8, 0.9, and 1.0. It should be noted that the other properties of GCCM are kept. The results show that the displacement of slope tends to decrease when the interface friction increase, as seen in Fig. 5-13. The effect of GCCM on deformation of slope is also reduced with depth.

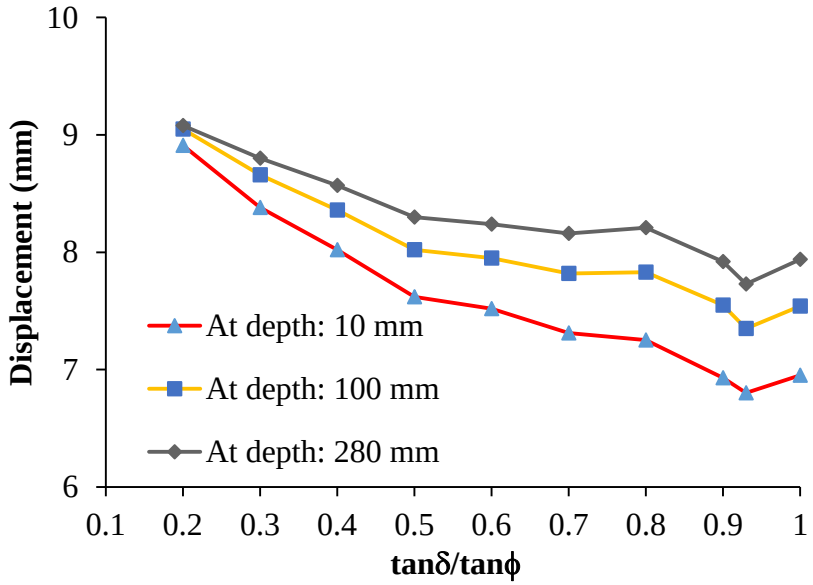

Fig. 5-13 Effect of the interface friction on the total displacement of slope reinforced with GCCM at section V3, when h_A = 250 mm

Based on the numerical simulation's results mentioned above, it could be said that the stiffness and the interface friction are crucial parameters of GCCM in term of slope stabilization.

5.4. Discussion

The increase of pore water pressure and hydraulic force induced by seepage flow causes the slope displacing and failure. The displacement of soil occurs throughout the slope with different magnitude. The soil movement is larger at the shallow depth and at the upslope compared to those of others location within the slope. The deformation of slope undergoing seepage flow is characterized into three stages: stable stage, moving stage, and failure stage. The transformation among these stages is identified by two sudden

change points, e.g., P_m and P_f. This implies that the slope has shown some signs, e.g., moving stage, before failure. According to Punongbayan R et al. (2002), the landslide occurred in Antipolo City, Philippines in 1999, which buried many houses in the area, had shown some signs such as cracks formed on the walls of houses several months before happening in August 1999.

To explain the mechanism of GCCM reinforcement, the stiffness of GCCM may be considered as a key factor. Because of the constrain at the downslope, e.g., the existence of retaining wall at the downslope, the deformation of slope can occur from the middle to upper slope in the tests. By considering the fact that (1) the relative stiffness of GCCM to the soil is large, and (2) the interface friction between GCCM and the soil is comparable to the internal friction of the soil as shown in the previous section, it can be said that the GCCM has a function to equalize the displacement near the slope surface along the slope. Because of this, the large deformation occurs in the mid-slope in Case 1, while the displacement equalization function of the GCCM makes the surface displacement smaller in Case 2. Moreover, total force induced by the GCCM weight acts on the slope and makes the effective stress increase. Consequently, the slope reinforced with GCCM is more stable.

The movement of soil including magnitude and direction at any location and time during the test could be measured by the PIV technique with the accuracy of 0.13 mm. Based on the movement of soil observed from PIV, the failure surface can be defined. It is noted that the PIV technique does not require putting any marker within the model slope. Therefore, the behavior of soil slope is not affected compared to the case of using tilt meter or accelerometer as a kind of inclinometer to measure the displacement (Orense et al., 2004; Sasahara, 2017). Buried sensors inside model slope may affect the behavior of soil movement (Zhang et al., 2009).

The results obtained from the numerical simulation confirm that the stiffness of GCCM and the interface friction play an important role in reinforcing the slope. However, the displacements and the depth of failure zone obtained from simulation and physical test are not consistent. It might come from the limitation of numerical simulation.

5.5 Remarks

Based on the two physical model tests of the sandy slope with and without GCCM and numerical simulation, some major remarks can be summarized as follows:

- GCCM could reinforce slope by contributing the displacement equalization function, friction force, and normal force on the slope surface. The stiffness of GCCM and the interface friction play an important role in reinforcing the slope. Consequently, the deformation of slope reinforced with GCCM is significantly smaller than that of the slope without GCCM.
- Three stages of deformation are observed which are steady stage, moving stage, and failure stage. These stages can be identified using a plot between displacement and water pressure head curve. In addition, the displacement of soil within slope reinforced with GCCM tends to increase from the surface to a certain depth, and then it tends to decrease by depth because of the effect of GCCM.
- The PIV technique works well for deformation measurement of slope. In this study, the accuracy of PIV technique reaches a value of 0.13 mm which is smaller than the 0.16 mm effective diameter (d_{10}) of sand.

Chapter 6: Centrifuge model testing results and discussion

In the centrifuge model tests, change of the pore water pressures and displacement of the soil slope are monitored. In this section, the pore water pressure and the horizontal displacement observed by PWP and ACC sensors are reported and interpreted.

6.1 Pore water pressure

In cases with seepage, water is supplied into the supply chamber through a 5 mm diameter plastic tube. The flow rate is adjusted using a valve outside the centrifuge chamber. Raise of the water level in the supply chamber is presented in Fig. 6-1. It can be seen that the difference between raising the water level in the cases without/with GCCM is quite small, so this small difference can be neglected.

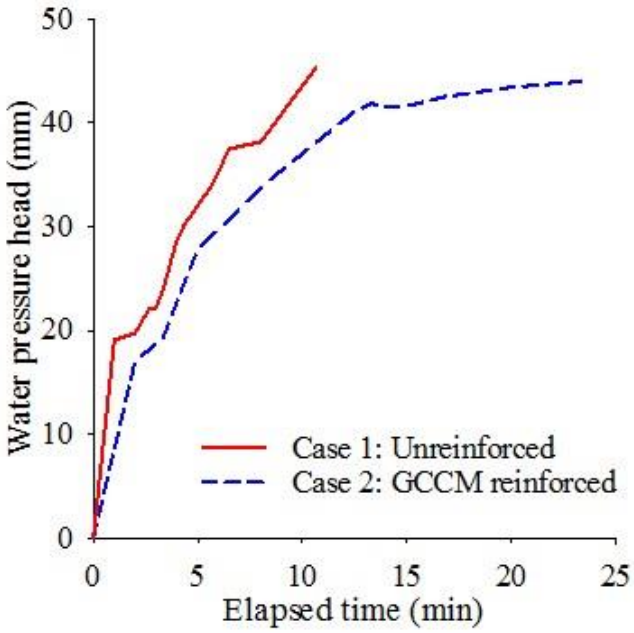

Fig. 6-1 Rise of water level in the supply chamber

Fig. 6-2 shows change of the water level at different moments during the test. At the beginning of the test, the water level is near the base of the slope. This indicates that the slope is not fully saturated. In other words, the real situation of a slope can be simulated. In cases with seepage, the water level is nearly parallel to the base (see Fig. 6-2(a), 6-2(b)). In contrast, the water level raises significantly near the toe in the cases with rainfall (see Fig. 6-2(c), 6-2(d)). This difference can be caused by the location of ‘water supply’, i.e., in the cases with seepage, the water supply is on the left boundary

of the slope, while in the cases with rainfall, the water supply is distributed along slope surface.

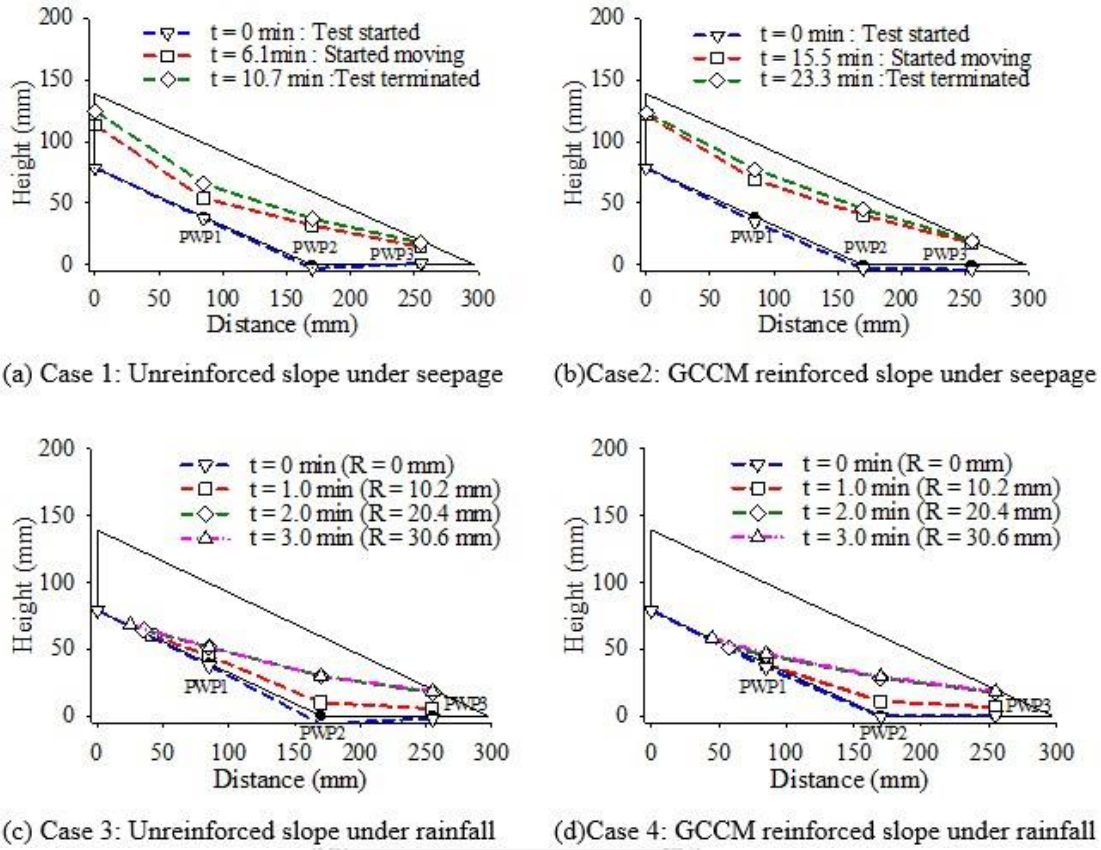

Fig. 6-2 Change of water level in soil slope with time

Fig. 6-3 shows the changes in the pore water pressure at PWP1 and discharge in the cases with rainfall. The rise of PWP1 in Case 4 is slower and smaller than that in Case 3. The reason can be attributed to the sealing function provided by the GCCM on the slope surface. In addition, discharge of water into the drainage tank is larger in the case with GCCM (Case 4). The larger discharge in the case with GCCM may come from the contribution of rainwater running off on the GCCM surface. These observations indicate that GCCM has reduced an amount of rainwater infiltrating into soil slope.

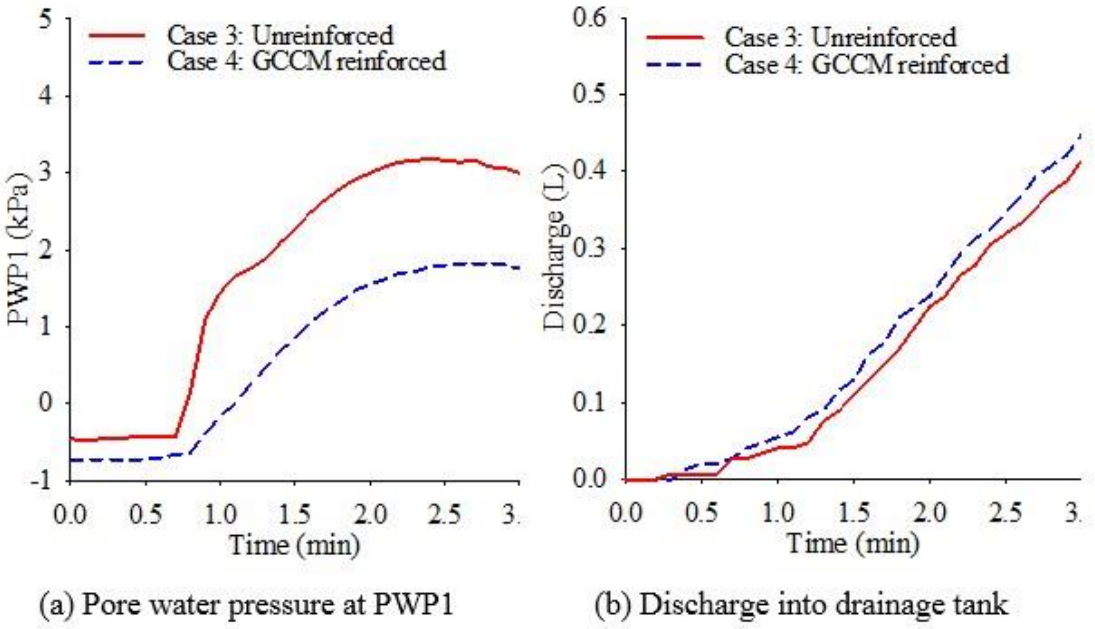

Fig. 6-3 Changes of water pressure at PWP1 and discharge from the slope in rainfall cases

6.2 Displacement

Based on the acceleration data measured from accelerometer sensors embedded within model slope, the horizontal movement of the slope can be estimated.

The horizontal displacement profiles at cross sections A (upslope), B (toe slope), and C (toe slope) are plotted in Fig. 6-4. In all cases, the horizontal displacements are dominated at the toe and near the surface of the slope. At the end of the tests, the maximum horizontal displacements observed are 5.7 mm (142.5 mm), 5.1 mm (127.5 mm), 1.6 mm (40.0 mm), and 0.15 mm (3.8 mm) for Case 1, 2, 3, and 4, respectively, as shown in Fig. 6-4. It should be noted that the values in brackets are values in the prototype.

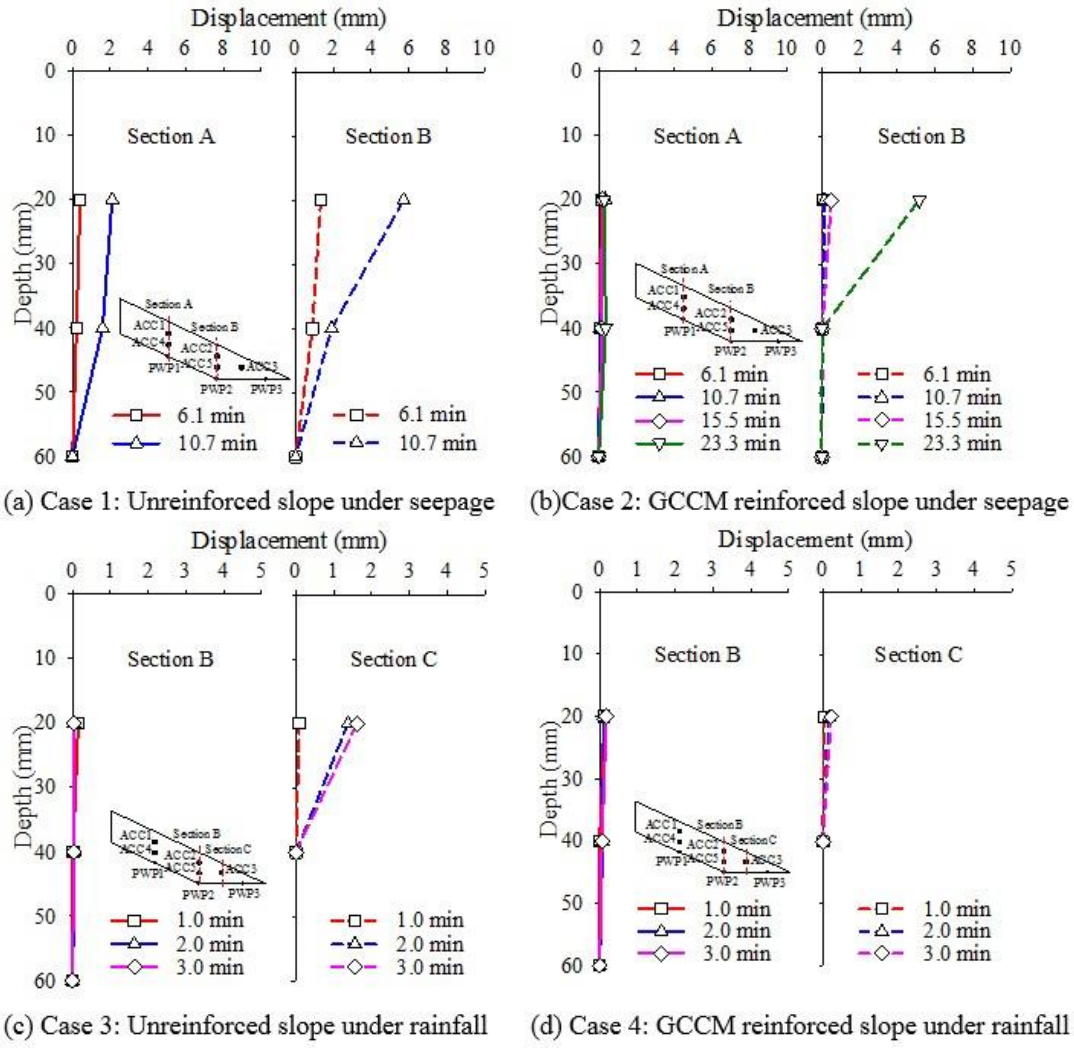

Fig. 6-4 Horizontal displacements of slope at different locations

In order to evaluate the benefit of GCCM, the change of pore water pressure at PWP2 and the horizontal displacement at ACC2 for Cases 1 and 2 and at ACC3 for Cases 3 and 4 with time are plotted in Fig. 6-5. In the cases of seepage, the unreinforced slope starts moving after 6.1 min or the pore water pressure at PWP2 reaches 8.5 kPa; in contrast, for the case with GCCM reinforcement it is observed the moving when the time reaches 15.5 min or the pore water pressure at PWP2 reaches 9.9 kPa as illustrated in Fig. 6-5(a). In the cases of rainfall, after 1.4 min (cumulative rainfall of 14.3 mm), the unreinforced slope starts moving with small displacement while the slope with GCCM reinforcement still insignificantly displaces after 3.0 min (cumulative rainfall of 30.6 mm) as shown in Fig. 6-5(b). These observations indicate that the GCCM has played a significant role in increasing slope stability.

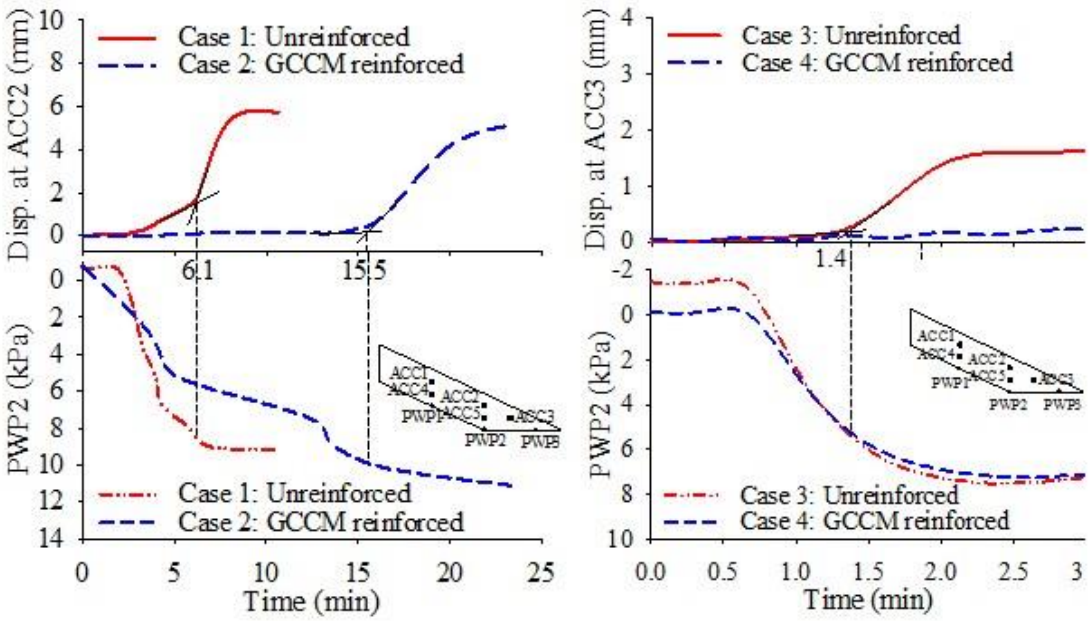

(a) Case 1 and 2: Seepage tests (b) Case 3 and 4: Rainfall tests

Fig. 6-5 Plots of water pressure and displacement versus time

Photos of the slopes after tests are presented in Fig. 6-6. It is noted that the dashed line is the original slope surface, the solid line is the slope surface when the test terminated. It can be seen that the failure zone of the unreinforced slope is larger than that of the case with GCCM under seepage as depicted by Figs. 6-6(a) and 6-6(b). For the rainfall case, small deformation is observed at the slope toe in the unreinforcement case, but no marked deformation is observed in the case with GCCM reinforcement as shown in Figs. 6-6(c) and 6-6(d). It is worth to note that the soil erosion is not observed during the test under rainfall.

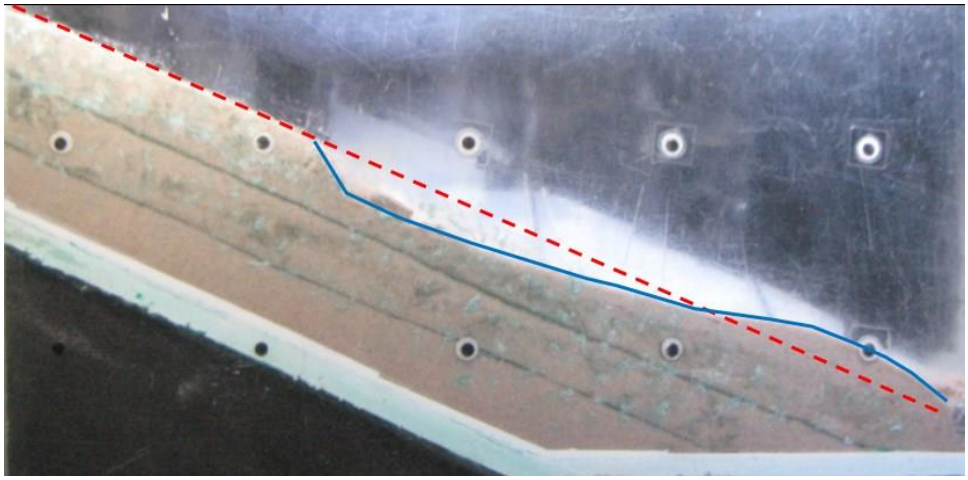

(a) Case 1: Unreinforced slope under seepage, t = 10.7 min

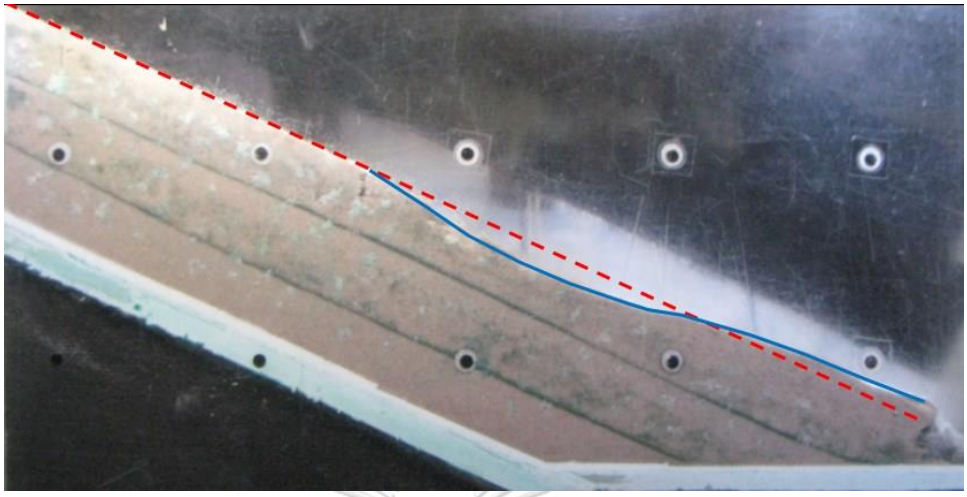

(b) Case2: GCCM reinforced slope under seepage, t = 23.3 min

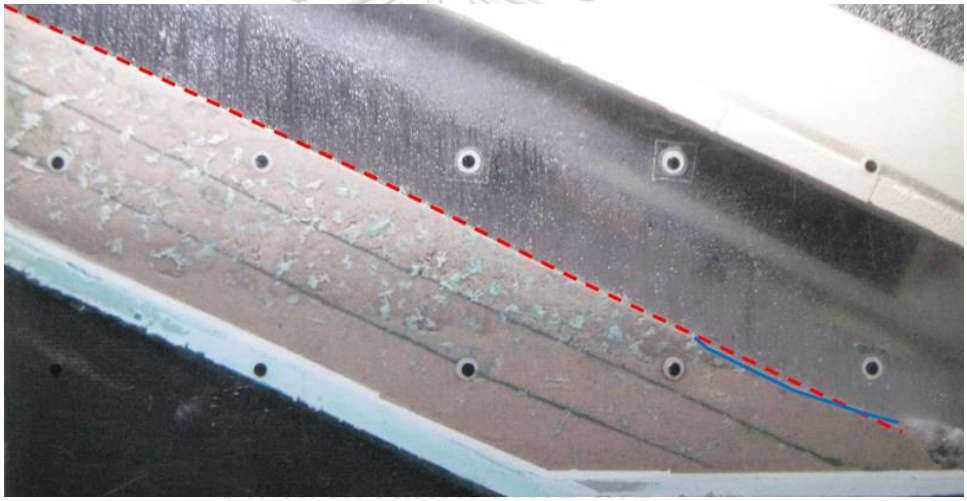

(c) Case 3: Unreinforced slope under rainfall, t = 3.0 min

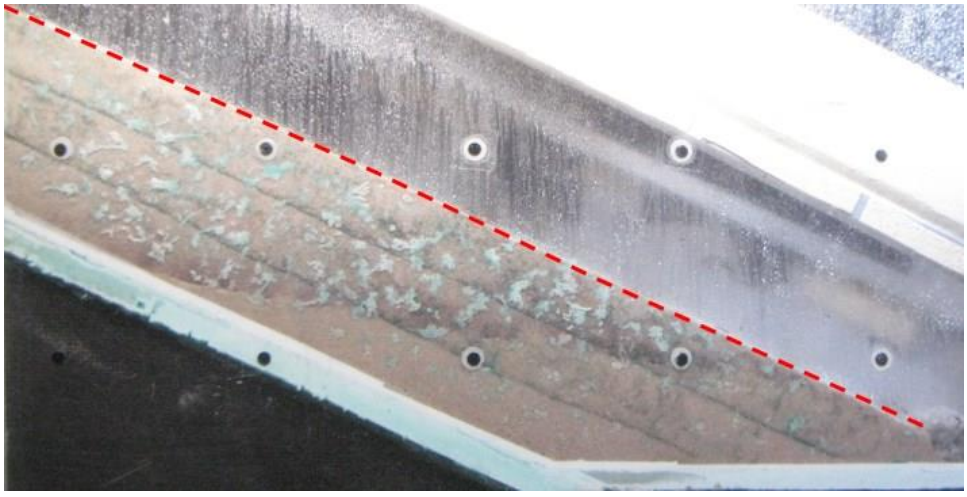

(d) Case 4: GCCM reinforced slope under rainfall, t = 3.0 min

Fig. 6-6 Side view of the slope when test terminated

6.3 Discussion

Comparing the deformation of the unreinforced slope under seepage (Fig. 6-4(a)) and under rainfall (Fig. 6-4(c)), it is interesting to note that in case of seepage, the deformation of slope occurs throughout the slope while in the case of rainfall the deformation occurs only near the slope toe. It may be attributed to the difference in the water level in the slope. In the case of seepage, the water level is nearly parallel to and developed along the entire base slope, whereas the rise of the water level in the case of rainfall is observed only near the slope toe.

Results of tests subjected to rainfall have shown that the GCCM can delay the increasing water pressure in the slope significantly as shown in Fig. 6. Although the coverage ratio of the GCCM is 75 %, the water pressure at the base slope (PWP1) is reduced by 44.7 % compared with the unreinforced case (see Fig. 6-3(a)). The sealing of the GCCM plays an important role against the infiltration of rainwater into the slope. The increase of water pressure induced by rainfall is one of the most factors causing slope instability. Especially to a real slope subjected to long and heavy rainfall, the effectiveness of GCCM on delaying increase of water level is very important.

Horizontal displacements of the slope under rainfall or seepage condition with the GCCM are significantly less than that of the unreinforced cases. In order to explain the mechanism of GCCM on slope reinforcement, the stiffness of GCCM and interface friction may be considered as key factors. Observation shows that the displacement of soil occurs mainly near the slope surface (i.e., less than 40 mm in the model or 1.0 m in the prototype) and the slope deformation tends to progress from the toe to the upper slope. By considering the fact that (1) the interface friction between the GCCM and sand is nearly equal to the frictional angle of the sand, and (2) the stiffness of the GCCM is very high compared to sand, it can be said that the GCCM can restrain the displacement of soil near the surface by its stiffness and friction resistance along GCCM-soil interface. In addition, the self-weight of GCCM can also help to increase the normal force and can introduce more friction force. Consequently, the slope reinforced by GCCM is more stable.

The combining the two functions, i.e., reinforcing and sealing function, might make the GCCM become a promising material for slope reinforcing, especially under the circumstance of climate change affecting seriously on slope stability.

6.4 Remarks

Based on the four centrifuge model tests of slope reinforced with and without the GCCM and subjected to seepage and rainfall, some remarks can be summarized as below:

- The deformation pattern of the slope subjected to seepage is different from that of the slope subjected to rainfall, i.e., deformation of the soil slope in the case of seepage tends to occur throughout the slope while is limited near the slope toe in the case of rainfall.
- The GCCM can help to reduce the displacement of the slope by its reinforcing function which comes from high stiffness and interfaces friction.
- The sealing effect of GCCM delays the increase of water pressure within the slope in the case of rainfall, so the hydraulic force acting on the soil slope is diminished.
- The combination of the two functions of GCCM such as reinforcement and sealing makes the slope reinforced with the GCCM more stable under rainfall.

Chapter 7: Conclusion and Recommendation

Based on the results of the tests on physical and mechanical properties of GCCM, the results of 1-g physical model tests and numerical simulation, and the results of 25-g centrifuge model tests, some conclusions can be drawn as follows.

- ✓ The properties of GCCM are uniform compared to other products that installed in the field because GCCM is manufactured in the factory. One of the important characteristics of GCCM is easy to install, and GCCM becomes a solid material with high stiffness and tensile strength after spraying water on its surface for a certain curing time due to the hydration of cement in GCCM. Additionally, the two geotextile layers located at the top and bottom of GCCM can resist the large strain caused by the external load during operation. Therefore, it can be expected that potential applications of GCCM in geotechnical engineering problems such as slope stabilization, erosion control, ditch lining, containment as a hydraulic barrier to water, etc., are plenty.
- ✓ The PIV technique works well for deformation measurement of the slope. In this study, the accuracy of PIV technique reaches a value of 0.13 mm which is smaller than the 0.16 mm effective diameter (d_{10}) of sand.
- ✓ Three stages of deformation are observed which are steady stage, moving stage, and failure stage. This can be identified from a plot between displacement and water pressure head curve. In addition, the displacement of soil within slope reinforced with GCCM tends to increase from the surface to a certain depth, and then it tends to decrease with depth, because of the effect of GCCM.
- ✓ The deformation pattern of the slope subjected to seepage is different from that of the slope subjected to rainfall, i.e., deformation of the soil slope in the case of seepage tends to occur throughout the slope while it is limited near the slope toe in the case of rainfall.

- ✓ The stiffness of GCCM and the interface friction play an important role in reinforcing the slope. The GCCM can help to reduce the displacement of the slope by its reinforcing function.
- ✓ The sealing effect of GCCM delays the increase of water pressure within the slope in the case of rainfall; therefore, the hydraulic force acting on the soil slope is diminished.
- ✓ The combination of the two functions of GCCM such as reinforcement and sealing makes the slope reinforced with the GCCM more stable under rainfall.

In this study, the performance of GCCM on reinforcing slope subjected to either rainfall or seepage condition is investigated. However, in reality, a real slope would be subjected to both of rainfall and seepage at the same time. Therefore, further studies on slope reinforced with GCCM under both seepage and rainfall are necessary. Additionally, this study demonstrates that GCCM has shown good performance on reinforcing slope with shallow depth, e.g., 1 – 2 m. Nevertheless, from the view of the overall stability of slope with deeper depth, the effectiveness of GCCM may be not significant and should be studied further.

REFERENCES

References

Abramson, L., Lee, T., Sharma, S., and Boyce, G. (2002). *Slope Stability and Stabilization Methods*, John Wiley, New York.

Adrian, R. J. (1991). "Particle-Imaging Techniques for Experimental Fluid Mechanics." *Annual Review of Fluid Mechanics*, 23, 261-304.

Ahn, T. B., Cho, S. D., and Yang, S. C. (2002). "Stabilization of soil slope using geosynthetic mulching mat." *Geotextiles and Geomembranes*, 20(2), 135-146.

Akay, O., Özer, A. T., Fox, G. A., Bartlett, S. F., and Arellano, D. (2013). "Behavior of sandy slopes remediated by EPS-block geofoam under seepage flow." *Geotextiles and Geomembranes*, 37, 81-98.

Andrawes, K. Z., and Butterfield, R. (1973). "The measurement of planar displacements of sand grains." *Géotechnique*, 23(4), 571-576.

Arthur, J. R. F., James, R. G., and Roscoe, K. H. (1964). "The Determination of Stress Fields During Plane of a Sand Mass." *Géotechnique*, 14(4), 283-308.

ASTM-D422-63 (1998). "Standard Test Method for Particle-Size Analysis of Soils." ASTM International, West Conshohocken, PA,.

ASTM-D3080-98 (1998). "Standard Test Method for Direct Shear Test of Soils Under Consolidated Drained Conditions." ASTM International, West Conshohocken, PA, USA.

ASTM-D5199 (2006). "Standard Test Method for Measuring the Nominal Thickness of Geosynthetics." ASTM International, West Conshohocken, PA, USA.

ASTM-D5993 (2014). "Standard Test Method for Measuring Mass Per Unit of Geosynthetic Clay Liners." ASTM International, West Conshohocken, PA, USA.

ASTM-D6768 (2006). "Standard Test Method for breaking force and elongation of textile fabrics." ASTM International, West Conshohocken, PA, USA.

Boonyanuphap, J. (2013). "Cost-benefit analysis of vetiver system-based rehabilitation measures for landslide-damaged mountainous agricultural lands in the lower Northern Thailand." *Natural Hazards*, 69(1), 599-629.

Bouazza, A. (2002). "Geosynthetic clay liners." *Geotextiles and Geomembranes*, 20(1), 3-17.

BS-EN-12467 (2012). "Fibre-cement flat sheets - Product specification and test methods." BSI Standards Limited, EUROPEAN COMMITTEE FOR STANDARDIZATION, Brussels.

Bush, D. I., Jenner, C. G., and Bassett, R. H. (1990). "The design and construction of geocell foundation mattresses supporting embankments over soft grounds." *Geotextiles and Geomembranes*, 9(1), 83-98.

Butterfield, R., Harkness, R. M., and Andrews, K. Z. (1970). "A Stero-Photogrammetric Method for Measuring Displacement Fields." *Géotechnique*, 20(3), 308-314.

Ceteau-LTD. (2014). "Natural sodium bentonite geosynthetic clay liner Ceuteau NP400."

Chen, H., Dadson, S., and Chi, Y.-G. (2006). "Recent rainfall-induced landslides and debris flow in northern Taiwan." *Geomorphology*, 77(1), 112-125.

Colombo, I. G., Magri, A., Zani, G., Colombo, M., and di Prisco, M. (2013). "Erratum to: Textile Reinforced Concrete: experimental investigation on design parameters." *Materials and Structures*, 46(11), 1953-1971.

Concrete_Canvas_Ltd. "Concrete Canvas." < **Error! Hyperlink reference not valid.**. (9 Dec, 2017).

Dainty, J. C. (1975). *Laser Speckle and Related Phenomena*, Springer-Verlag Berlin Heidelberg.

Daniel, D. E., Koerner, R. M., Bonapart, R., Landreth, R. E., Carson, D. A., and Scranton, H. B. (1998). " Slope Stability of Geosynthetic Clay Liner Test Plots." *Journal of Geotechnical and Geoenvironmental Engineering*, 124(7), 628-637.

Day, R. W., and Axten, G. W. (1989). "Surficial stability of compacted clay slopes." *Journal of Geotechnical Engineering*, 115(4), 577–580.

Donat, M. G., Lowry, A. L., Alexander, L. V., O'Gorman, P. A., and Maher, N. (2016). "More extreme precipitation in the world's dry and wet regions." *Nature Climate Change*, 6, 508.

Eab, K. H., Likitlersuang, S., and Takahashi, A. (2015). "Laboratory and modelling investigation of root-reinforced system for slope stabilisation." *Soils and Foundations*, 55(5), 1270-1281.

Eab, K. H., Takahashi, A., and Likitlersuang, S. (2014). "Centrifuge modelling of root-reinforced soil slope subjected to rainfall infiltration." *Géotechnique Letters*, 4(3), 211-216.

Evans, D. A. (1972). "Slope Stability Report." Slope Stability Committee, Department of Building and Safety, Los Angeles, CA.

Fangyu, H., Huisu, C., Wulong, Z., Tao, L., and Yujie, Y. (2014). "Influence of 3D spacer fabric on drying shrinkage of concrete canvas." *Journal of Industrial Textiles*, 45(6), 1457-1476.

Fangyu, H., Huisu, C., Xiangyu, L., Buchuan, B., Tao, L., Wulong, Z., and Wen Hui, D. (2015). "Improvement of mechanical properties of concrete canvas by anhydrite-modified calcium sulfoaluminate cement." *Journal of Composite Materials*, 50(14), 1937-1950.

Fowler, J., and Koerner, M. "Stabilization of Very Soft Soils Using Geosynthetics." *Proc., Proceedings of the Geosynthetics '87*, 289–300.

Fowze, J. S. M., Bergado, D. T., Soralump, S., Voottipreux, P., and Dechasakulsom, M. (2012). "Rain-triggered landslide hazards and mitigation measures in Thailand: From research to practice." *Geotextiles and Geomembranes*, 30, 50-64.

Fuchu, D., Lee, C. F., and Sijing, W. (1999). "Analysis of rainstorm-induced slide-debris flows on natural terrain of Lantau Island, Hong Kong." *Engineering Geology*, 51(4), 279-290.

Gilbert, R. B., and Wright, S. G. (2010). "Slope stability with geosynthetic clay liners." *Geosynthetic Clay Liners for Waste Containment Facilities*, CRC Press, 169-202.

Guzzetti, F., Cardinali, M., Reichenbach, P., Cipolla, F., Sebastiani, C., Galli, M., and Salvati, P. (2004). "Landslides triggered by the 23 November 2000 rainfall event in the Imperia Province, Western Liguria, Italy." *Engineering Geology*, 73(3), 229-245.

Han, F., Chen, H., Jiang, K., Zhang, W., Lv, T., and Yang, Y. (2014). "Influences of geometric patterns of 3D spacer fabric on tensile behavior of concrete canvas." *Construction and Building Materials*, 65, 620-629.

Hansen, M. J. (1984). "Strategies for classification of landslides." *Slope instability*, D. Brunsden, and D. B. Prior, eds., Wiley, Chichester, 1-25.

Hegger, J., and Voss, S. (2008). "Investigations on the bearing behaviour and application potential of textile reinforced concrete." *Engineering Structures*, 30(7), 2050-2056.

Hu, Y., Zhang, G., Zhang, J.-M., and Lee, C. F. (2010). "Centrifuge modeling of geotextile-reinforced cohesive slopes." *Geotextiles and Geomembranes*, 28(1), 12-22.

Huang, C. C., Yih-Jang, J., Lih-Kang, H., and Jin-Long, L. (2009). "Internal soil moisture and piezometric responses to rainfall-induced shallow slope failures." *Journal of Hydrology*, 370(1), 39-51.

Huang, C. C., and Yuin, S. C. (2010). "Experimental investigation of rainfall criteria for shallow slope failures." *Geomorphology*, 120(3-4), 326-338.

Intarawichian, N., and Dasananda, S. (2011). "Frequency ratio model based landslide susceptibility mapping in lower Mae Chaem watershed, Northern Thailand." *Environmental Earth Sciences*, 64(8), 2271-2285.

ISO-12236 (2013). "Geosynthetic static puncture test."Bureau of Indian Standards: India.

Jiang, M. J., Konrad, J. M., and Leroueil, S. (2003). "An efficient technique for generating homogeneous specimens for DEM studies." *Computers and Geotechnics*, 30(7), 579-597.

Jiao, J. J., Wang, X.-S., and Nandy, S. (2005). "Confined groundwater zone and slope instability in weathered igneous rocks in Hong Kong." *Engineering Geology*, 80(1), 71-92.

Jongvivatsakul, P., Ramdit, T., Ngo, T. P., and Likitlersuang, S. (2018). "Experimental investigation on mechanical properties of geosynthetic cementitious composite mat (GCCM)." *Construction and Building Materials*, 166, 956-965.

Khamfong, K., Navanugraha, C., Junggoth, R., and Wongchantra, P. (2013). "The development geo-information technology on flood and landslide preventing and solving for the local government at Uttaradit Province, Thailand." *Research Journal of Applied Sciences*, 8(3), 148-151.

Ladd, R. S. (1978). "Preparing test specimens using undercompaction." *Geotechnical Testing Journal*, 1(1), 16-23.

Lehmann, J., Coumou, D., and Frieler, K. (2015). "Increased record-breaking precipitation events under global warming." *Climatic Change*, 132(4), 501-515.

Lumb, P. (1975). "Slope failures in Hong Kong." *Quarterly Journal of Engineering Geology and Hydrogeology*, 8(1), 31-65.

Luo, F., Zhang, G., Liu, Y., and Ma, C. (2018). "Centrifuge modeling of the geotextile reinforced slope subject to drawdown." *Geotextiles and Geomembranes*, 46(1), 11-21.

Madabhushi, G. (2014). *Centrifuge Modelling for Civil Engineers*, CRC Press, London.

Mafian, S., Huat, B. B. K., Rahman, N. A., and Singh, H. (2009). "Potential plant species for live pole application in tropical environment." *American Journal of Environmental Sciences*, 5(6), 759-764.

Ng, C. W. W., Kamchoom, V., and Leung, A. K. (2015). "Centrifuge modelling of the effects of root geometry on transpiration-induced suction and stability of vegetated slopes." *Landslides*.

Ono, K., Kazama, S., and Ekkawatpanit, C. (2014). "Assessment of rainfall-induced shallow landslides in Phetchabun and Krabi provinces, Thailand." *Natural Hazards*, 74(3), 2089-2107.

Orense, R., Shimoma, S., Maeda, K., and Towhata, I. (2004). "Instrumented Model Slope Failure due to Water Seepage." *Journal of Natural Disaster Science*, 26(1), 15-26.

Paikowsky, S., and Xi, F. (2000). "Particle Motion Tracking Utilizing a High-Resolution Digital CCD Camera." *Geotechnical Testing Journal*, 23(1), 123-134.

Peng, J., Fan, Z., Wu, D., Zhuang, J., Dai, F., Chen, W., and Zhao, C. (2015). "Heavy rainfall triggered loess–mudstone landslide and subsequent debris flow in Tianshui, China." *Engineering Geology*, 186(Supplement C), 79-90.

Punongbayan R, S., Arboleda R, A., Bornas M, V., and Abigania M, T. (2002). "The 3 August 1999 Cherry Hills Landslide in Antipolo City, Philippines." *Landslide News*, 13, 12-15.

Rahardjo, H., Leong, E. C., and Rezaur, R. B. (2008). "Effect of antecedent rainfall on pore-water pressure distribution characteristics in residual soil slopes under tropical rainfall." *Hydrological Processes*, 22(4), 506-523.

Raisinghani, D. V., and Viswanadham, B. V. S. (2011). "Centrifuge model study on low permeable slope reinforced by hybrid geosynthetics." *Geotextiles and Geomembranes*, 29(6), 567-580.

Rajabian, A., and Viswanadham, B. V. S. (2016). "Behaviour of anchored geosynthetic-reinforced slopes subjected to seepage in a geotechnical centrifuge." *Geosynthetics International*, 23(1), 36-47.

Rajabian, A., Viswanadham, B. V. S., Ghiassian, H., and Salehzadeh, H. (2012). "Centrifuge model studies on anchored geosynthetic slopes for coastal shore protection." *Geotextiles and Geomembranes*, 34, 144-157.

Raymond, G. P., Giroud, J. P., International Society of Soil, M., Foundation, E., Technical Committee Tc, G., and Geosynthetics (1993). *Geosynthetics case histories*, International Society for Soil Mechanics and Foundation Engineering; BiTech Publishers, [S.l.]; Richmond, B.C.

Roscoe, K. H., Arthur, J. R. F., and James, R. G. (1963). "Determination of Strains in Soils by X-ray Method." *Civil Engineering and Public Works Review*, 58, 873-876.

Sasahara, K. (2017). "Prediction of the shear deformation of a sandy model slope generated by rainfall based on the monitoring of the shear strain and the pore pressure in the slope." *Engineering Geology*, 224, 75-86.

Sharma, J. S., and Bolton, M. D. (1996). "Centrifuge modelling of an embankment on soft clay reinforced with a geogrid." *Geotextiles and Geomembranes*, 14(1), 1-17.

Soralump, S. (2010). "Rainfall-triggered landslide: From research to mitigation practice in Thailand." *Geotechnical Engineering*, 41(1).

Takemura, J., Kondoh, M., Esaki, T., Kouda, M., and Kusakabe, O. (1999). "Centrifuge model tests on double propped wall excavation in soft clay." *SOILS and FOUNDATIONS*, 39(3), 75-87.

Taylor, R. N., Grant, R. J., Robson, S., and Kuwano, J. "An image analysis system for determining plane and 3-D displacements in soil models." *Proc., Proceedings of the International Conference Centrifuge 98*, 73-78.

Taylor, Z. J., Gurka, R., Kopp, G. A., and Liberzon, A. (2010). "Long-Duration Time-Resolved PIV to Study Unsteady Aerodynamics." *Instrumentation and Measurement*, 59(12), 3262-3269.

Thusyanthan, N. I., Madabhushi, S. P. G., and Singh, S. (2007). "Tension in geomembranes on landfill slopes under static and earthquake loading—Centrifuge study." *Geotextiles and Geomembranes*, 25(2), 78-95.

Titi, H., and Helwany, S. (2007). "Investigation of vertical members to resist surficial slope instabilities, (WHRP 07–03). Wisconsin Department of Transportation, Madison, WI.".

Tsesarsky, M., Peled, A., Katz, A., and Anteby, I. (2013). "Strengthening concrete elements by confinement within textile reinforced concrete (TRC) shells – Static and impact properties." *Construction and Building Materials*, 44, 514-523.

US-Army-Corps-of-Engineers (1995). *Standard Practice for Shotcrete*, American Society of Civil Engineers, New York.

Viswanadham, B. V. S., and König, D. (2009). "Centrifuge modeling of geotextile-reinforced slopes subjected to differential settlements." *Geotextiles and Geomembranes*, 27(2), 77-88.

Wang, L., Zhang, G., and Zhang, J.-M. (2011). "Centrifuge model tests of geotextile-reinforced soil embankments during an earthquake." *Geotextiles and Geomembranes*, 29(3), 222-232.

Wang, L., Zhang, G., and Zhang, J. M. "Centrifuge modeling of failure behavior of pile-reinforced slope." *Proc., 14th Asian Regional Conference on Soil Mechanics and Geotechnical Engineering*.

White, D. J., Take, W. A., and Bolton, M. D. (2003). "Soil deformation measurement using particle image velocimetry (PIV) and photogrammetry." *Géotechnique*, 53(7), 619-631.

Wu, K. J., and Austin, D. N. (1992). "Three-dimensional polyethylene geocells for erosion control and channel linings." *Geotextiles and Geomembranes*, 11(4), 611-620.

Wu, T. H. (1994). "Slope stabilization using vegetation." *Geotechnical engineering: emerging trends in design and practice*, 377-403.

Wu, T. H., Kokesh, C. M., Trenner, B. R., and Fox, P. J. (2014). "Use of live poles for stabilization of a shallow slope failure." *Journal of Geotechnical and Geoenvironmental Engineering*, 140(10).

Yan, S. W., and Chu, J. (2010). "Construction of an offshore dike using slurry filled geotextile mats." *Geotextiles and Geomembranes*, 28(5), 422-433.

Yasuhara, K., Komine, H., Murakami, S., Chen, G., Mitani, Y., and Duc, D. M. (2012). "Effects of climate change on geo-disasters in coastal zones and their adaptation." *Geotextiles and Geomembranes*, 30, 24-34.

Zhang, F., Chen, H., Li, X., Li, H., Lv, T., Zhang, W., and Yang, Y. (2017). "Experimental study of the mechanical behavior of FRP-reinforced concrete canvas panels." *Composite Structures*, 176, 608-616.

Zhang, G., Hu, Y., and Zhang, J. M. (2009). "New image analysis-based displacement-measurement system for geotechnical centrifuge modeling tests." *Measurement*, 42(1), 87-96.

APPENDIX

VITA